Elasto-damage mechanics of osteons: A bottom-up multiscale approach

Pierfrancesco Gaziano*[a], Elisabetta Monaldo[b], Cristina Falcinelli[c], Giuseppe Vairo[a]

[a] *Department of Civil Engineering & Computer Science (DICII), University of Rome "Tor Vergata", Via del Politecnico 1, 00133 Rome, Italy*
[b] *Department of Engineering, Roma Tre University, Via Vito Volterra 62, 00146 Rome, Italy*
[c] *Department of Engineering and Geology (InGeo), G. D'Annunzio Chieti-Pescara University, Viale Pindaro 42, 65127 Pescara, Italy*

Abstract

In this paper, a multiscale rationale is applied to develop a bottom-up modelling strategy for analyzing the elasto-damage response of osteons, resulting in a first step towards a refined mechanical description of cortical bone tissue at the macroscale. Main structural features over multiple length scales are encompassed. A single osteon is described by considering a multi-layered arrangement of cylindrical lamellae and accounting for both lacunar microvoids and thin interlamellar regions, these latter modelled as soft interfaces. A multi-step homogenization procedure has been conceived and numerically applied to describe the equivalent mechanical response of osteon constituents, upscaling dominant subscale mechanisms. A progressive stress-based damage approach has been implemented via a finite-element technique, allowing to describe interlaminar and/or intralaminar brittle failure modes. Proposed approach has been successfully validated by numerically reproducing available experimental tests of isolated osteons under different loading conditions. Present histologically-oriented multiscale model revealed to be sound and consistent, opening towards further insights about the influence on bone biomechanics of through-the-scales biophysical/biochemical alterations, possibly related to ageing or diseases.

Keywords: Bone micromechanics, multiscale modelling, numerical homogenization, damage-based finite-element formulation, osteon mechanics

*Corresponding Author Email address: gaziano@ing.uniroma2.it (P. Gaziano).

1. Introduction

Bone is a complex heterogenous material consisting of different organized hierarchical structures over multiple length scales [1]. All the bone constituents are combined in a remarkably effective way so as to form a properly-organized and nature-optimized material with superior mechanical properties combining high stiffness, strength and toughness [2, 3]. At the organ level, two distinct types of bone tissues, characterized by different mechanical properties, can be distinguished, namely the cortical (or compact) bone, dense and stiff, and the trabecular (or spongy) bone, porous and tough [4, 5]. Stiffness and loading-bearing capacity of bone structures are mainly associated to cortical tissue. At the microscale, cortical bone is constituted by hollow quasi-cylindrical systems, called osteons or Haversian systems [4, 6, 7], running approximately parallel to the main direction of the bone structure. Osteons have an average diameter in the range of $200 \div 250$ µm and are characterized by a central canal (called Haversian canal) having diameter in the order of 40 µm (see Fig. 1). At an intermediate subscale between the micro- and the nano-scale, osteons are made up of several coaxial pseudo-cylindrical layers, about 3 µm in thickness and wrapping around the Haversian canal, called lamellae [5, 8]. Each lamella exhibits a defined pattern of sub-microstructural units (the so-called sublamellae), characterized by an ordered arrangement of mineralized collagen fibrils (MCF). [8, 9]. In turn, at the nanoscale, MCFs are constituted by Type-I collagen fibrils strengthened by crystals of a mineral phase mainly constituted by hydroxyapatite (HA). Minor quantities of water, non-collagenous organic proteins (NCPs) and impurities are also present [1, 6, 10, 11].

Bone material composition and structural organization at each length scale highly affect its mechanical behaviour and failure mechanisms at the macroscale level. In this framework, it is well-documented that bone is characterized by an anisotropic constitutive response, and that osteons were proved to have a key role for the propagation of cracks at organ level [12–14]. As such, a proper understanding of onset and evolution of bone fracture mechanisms at the macroscale requires a suitable characterization of osteon mechanics and related damage features [7, 15].

To this aim, a consistent multiscale rationale, able to account for the histological arrangement of tissue constituents through multiple length scales, revealed to be highly effective for accurately investigating the mechanical response of biological tissues [16–23]. Since a structured multiscale strategy

(differently from phenomenological approaches) is defined via model parameters with a clear physical meaning, it also allows to describe the influence of possible physiopathological alterations related to ageing or diseases by straightforwardly setting such parameters through consistent histological evidence [24–28].

Finite Element (FE) modelling represents an effective tool for investigating bone biomechanics in health and disease at both the macro- and micro-scale [29–35]. However, at present only few FE-based models have been developed with the aim of describing the micromechanical behaviour of osteonal elements. Hogan [32] and Crolet et al. [33] were among the first researchers proposing estimates of compact bone equivalent elastic properties through FE-based micromechanical approaches. In particular, Hogan [32] investigated the dependence of the elastic moduli on the material properties of osteon substructures, finding a reasonable agreement with available experimental data. Crolet et al. [33] conducted a similar study by accounting for collagen/HA distribution within osteonic lamellae, in the framework of a multiscale approach. Their results, furnished however only in terms of bone homogenized elastic properties, showed good agreement with the experimental data, corroborating the hypothesis of periodicity of collagen/HA distribution within each single osteonic lamella.

A more detailed numerical model of a single osteon was developed by Prendergast and Huiskes [34], who investigated whether damage generates strains which may trigger bone remodeling processes. The authors provided important and useful evidence that local changes in the strain field are strictly related to the presence of microdamage and lacunar voids in Haversian bone microstructure. Nonetheless, the existence of damage was therein assumed a priori, not querying where and when the damage develops and evolves. In the studies of Guo et al. [36] and Najafi et al. [37], linearly-elastic fracture mechanics theory was employed to assess the role of microcracks at a single-osteon level, as well as their influence on the mechanical behaviour of cortical bone. However, their model revealed several limitations, since microstructural features of osteons were disregarded, and the assumption of homogeneous linearly-elastic materials was made. Hamed and Jasiuk [2] numerically investigated the bone strength at multiple length scales by modelling damage onset and propagation through the cohesive element technique. The authors provided some evidence contributing towards the understanding of bone sub-macroscale failure mechanisms. Nonetheless, although constitutive microscale arrangement was considered to a certain extent, fracture mech-

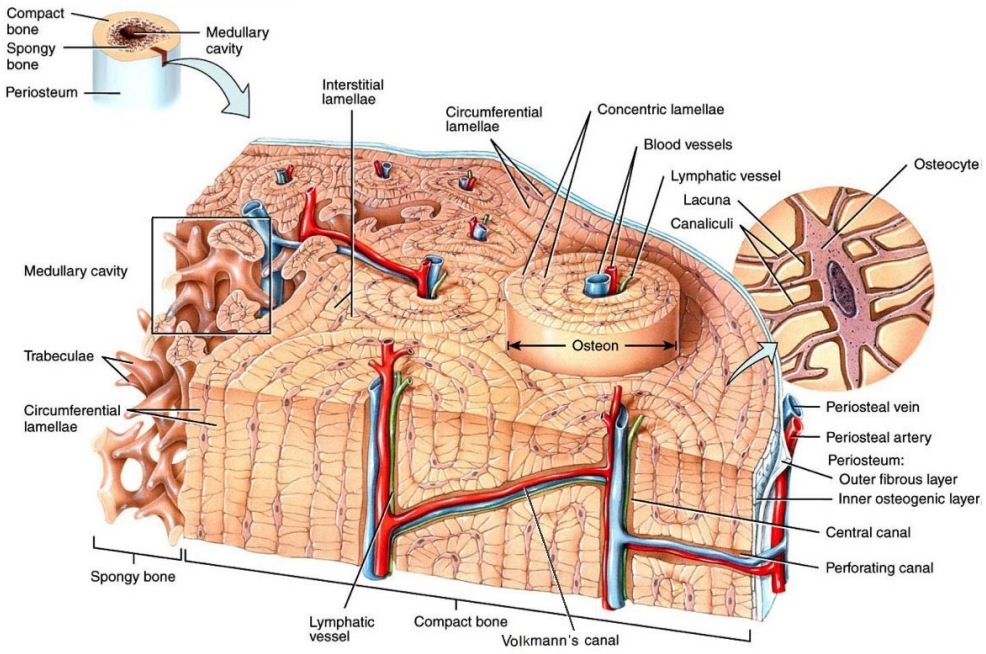

Figure 1: Illustrative sketch of the main histological aspects of cortical bone. The osteonal structure is evidenced together with all its characteristic features. Courtesy from `https://sciencediagrams.com/osteon/`.

anisms were driven by a-priori-defined initiation sites. Moreover, numerical models at different scales were decoupled each other, in the sense that mechanical features of bone structures at a given length scale were obtained not accounting for tissue features and structural organization at lower scales. More recently, Giner et al. [35] developed a multiscale numerical model of a single osteon, investigating microdamage onset and evolution. Thereinproposed results, associated to a radial compressive loading scenario, were succesfully compared with experimental test carried out by Ascenzi et al. [38]. However, the structural model of Giner et al. [35], and in fact all the other previously-described ones, considered a planar section of the actual three dimensional osteonal structure as a simplifying assumption, thus allowing only for an in-plane strain and stress analysis.

To the best of the authors' knowledge, a detailed three-dimensional multiscale model accounting for coupled through-the-scales mechanical responses up to the failure is still lacking. Accordingly, present paper aims to propose a novel histological-based description of single osteons by accounting for three-dimensional multiscale structural arrangement, based on a bottom-up (from nano- to micro-scale) formulation. In depth, a refined constitutive description, also encompassing a multistep homogenization procedure, has been conceived and employed to identify dominant mechanical response of osteonal constituents at different scales. A progressive damage formulation allowing to describe interlaminar and/or intralaminar brittle failure modes, has been conceived and applied to model osteonal elasto-damage response and failure mechanisms. Proposed model has been implemented through a FE technique and it has been successfully validated by replicating available experimental tests carried out under different loading conditions [39–41]. Obtained results highlight soundness and accuracy of the proposed approach, that can therefore be considered as useful for understanding how microdamage processes affect the overall mechanical behaviour of cortical bone, also accounting for disease- or ageing-induced structural and morphological alterations through different length scales. In such a way, enhanced novel multiscale strategies could be developed up to the macroscale, furnishing suitable indications for the proper assessment of bone fracture risk, and thereby allowing for possible clinical applications related to effective etiology identification, diagnosis and treatment of bone-related pathologies.

2. Single osteon model

2.1. Problem statement

The osteon is described as a perfectly cylindrical hollow body occupying the region Ω in the three-dimensional Euclidean space $\mathcal{E}^3$, having length L and inner and outer diameters D_H and D_O, respectively (see Fig. 2). The osteon is considered to be made up by a sequence of N coaxially-arranged units, called lamellae, and of $N-1$ interlamellar interfaces, modelling the very thin interlamellar zones located in between them. Because of this geometrical organization, a cylindrical coordinate system (r, θ, z) is conveniently introduced, with the origin O placed at the center of one of the osteon basis and the z-axis coincident with the cylinder axis (see Fig. 2).

From a histological standpoint, an actual osteonal structure additionally includes Volkmann canals, a cement line delimiting the single osteon

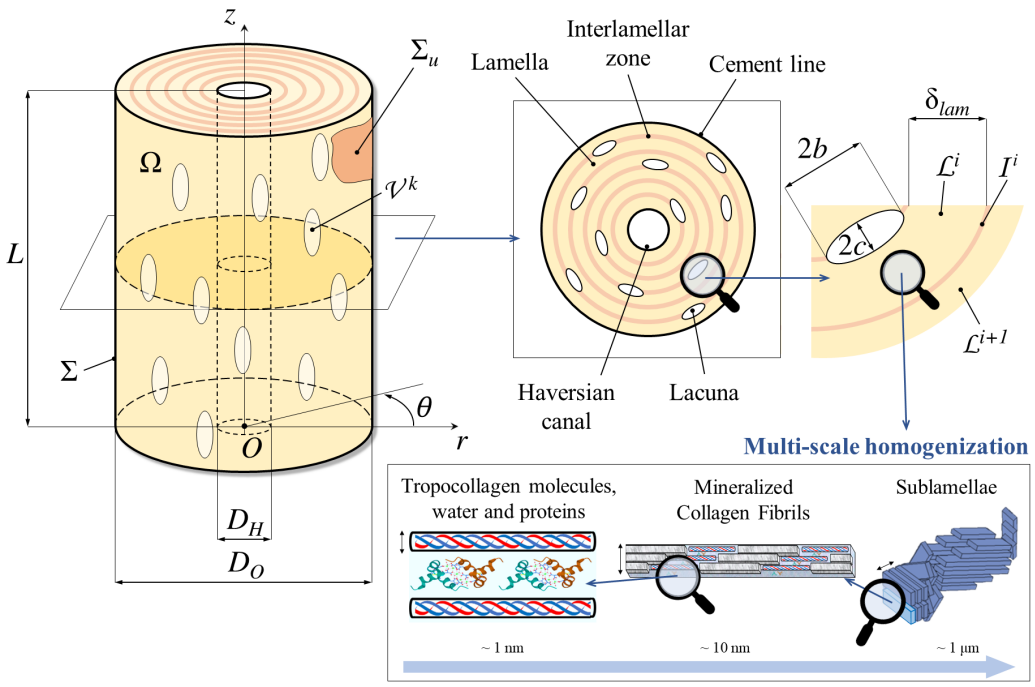

Figure 2: Osteon multiscale model. Geometrical and microstructural features: notation.

from the remaining cortical tissue, a fine network of canaliculi (the so-called syncytium, see Fig. 1), as well as lacunae. These latter are small cavities hosting the osteocytes (i.e., quiescent osteoblasts, the cells which secret the osteonal tissue), and which are mainly located at the interlamellar regions in a quite random fashion [1]. Following the evidence reported in [42], lacunae are herein modelled as homogeneously-distributed ellipsoidal-shaped void domains, all of them having length of the semi-axes equal to a, b, c, where $c < b < a$. Moreover, lacunar domains are oriented in such a way that the longest semi-axis is parallel to z and the shortest one is parallel to r. The number of lacunae N_l is chosen such that their volume fraction f_l within the osteonal domain lies in the range $1 \div 3\%$, which is a representative value for mature and healthy cortical tissue [1]. In detail, lacunae volume fraction f_l is related to N_l through the following relationship:

$$f_l = \frac{16\, N_l\, a\, b\, c}{3\,(D_O^2 - D_H^2)\, L} \tag{1}$$

In this work only the presence of lacunae has been considered. This choice follows the approach commonly adopted by other authors (e.g., [35]), since it is widely accepted that canaliculi and Volkmann canals play a secondary role in comparison to lacunae, these latter being much more abundant and larger. In addition, the influence of cement line becomes significant only if the mechanical behaviour of a set of more than one osteon is addressed, which is not the case herein considered. Note that the adopted hypotheses are perfectly in-line with the experimental tests carried out by Ascenzi and his coworkers, to which reference is made [39–41]. Such test were indeed conducted on single osteons (hence, without cement lines) having a shape just slightly deviating from the perfectly cylindrical one, not showing the presence of Volkmann canals and which were prepared by removing all the soft tissues.

For what follows it is useful to introduce some notation rules. In particular, with reference to Fig. 2, let symbol $\mathcal{V}^k$ denote the k-th lacunar void domain, with $k = 1, \dots, N_l$. Let additionally denote with $\mathcal{L}^i$ (with $i = 1, \dots, N$) and $\mathcal{I}^i = \partial\mathcal{L}_i \cap \partial\mathcal{L}_{i+1}$ (with $i = 1, \dots, N-1$) the material domains occupied by the i-th lamella and the i-th interlamellar interface, respectively. By defining overall domains $\mathcal{L} := \cup_{i=1}^{N} \mathcal{L}^i$, $\mathcal{I} := \cup_{i=1}^{N-1} \mathcal{I}^i$, and $\mathcal{V} := \cup_{k=1}^{N_l} \mathcal{V}^k$, the region Ω thereby results in $\Omega = \mathcal{L} \cup \mathcal{V}$. Furthermore, let $\Sigma := \partial\Omega$ be the boundary of the osteon region (comprising the ending bases, the inner surface of the innermost lamella and the outer surface of the outermost one). In particular, symbols Σ_p and Σ_u denote the disjoint portions of Σ on which tractions $\mathbf{p}$ and displacements $\mathbf{u}$ are prescribed, respectively, as detailed in the following.

2.2. Constitutive description: a multiscale rationale

The constitutive behaviour of osteonal tissue is described by neglecting any viscous and fluid effect. Osteonal structure is regarded as a composite medium including two different phases: the lamellar phase and the interlamellar one. In turn, lamellae are characterized by a precise microstructure defined by a specific hierarchical arrangement of collagen and hydroxyapatite. The constitutive behaviour of lamellar tissue is modelled in the framework of a multiscale approach, based on a bottom-up multi-step homogenization procedure. The homogenized responses of mineralized collagen fibrils and of a single osteonic lamella are numerically derived by considering specific representative unit cells. Numerical procedures have been implemented through customized codes in Matlab environment (Matlab v. R2018a, MathWorks,

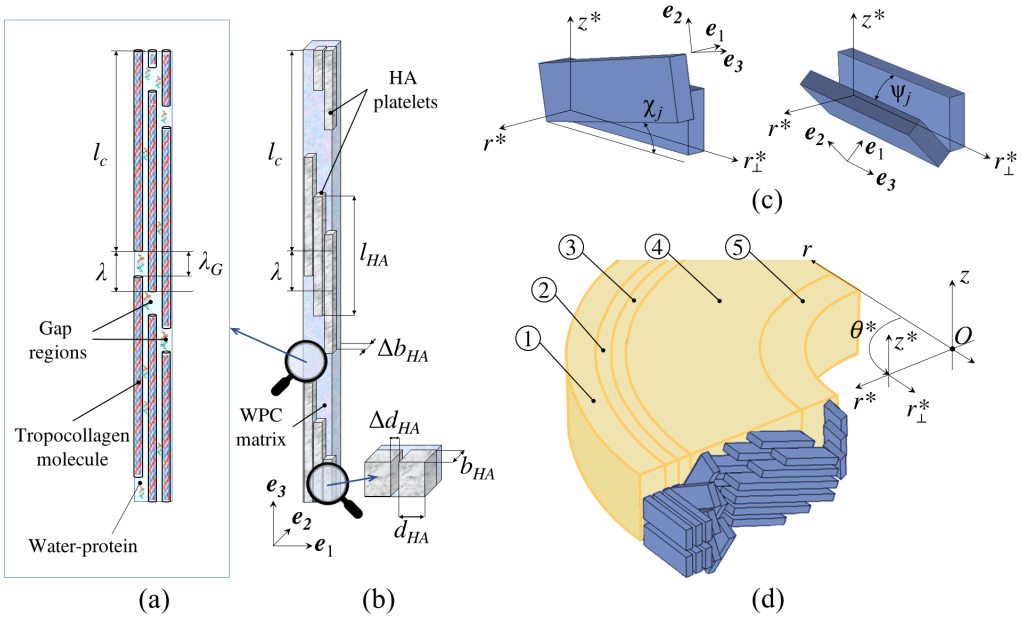

Figure 3: The Mineralized Collagen Fibrils (MCFs) and their arrangement within the lamellar structure. (a) Hodge-Petruska scheme describing the geometrical organization of tropocollagen molecules immersed in a water-protein matrix. (b) Platelet-shaped HA crystals originating within the collagen gap regions. (c) Angles χ_j and ψ_j of MCFs with respect to the local reference system $\{r^*, r_\perp^*, z^*\}$. (d) MCFs arrangement within the sublayers constituting a typical osteonic lamella.

MA, USA) integrated within the FE solver Comsol Multiphysics (Comsol with Matlab, v.5.4 COMSOL, Stockholm, Sweden).

2.2.1. Nanoscale: mineralized collagen fibrils

The basic building blocks of cortical bone at the nanoscale are Type-I collagen, hydroxyapatite (HA) crystals and small quantities of water and non-collagenous proteins (NCPs), which together form the so-called mineralized collagen fibrils (MCFs). These latter result from a mineralization process of simple collagen fibrils, which are made up of staggered arrays of tropocollagen molecules. With reference to Fig. 3(a), tropocollagen molecules, having length ℓ_c in unmineralized conditions, are arranged following the well-known Hodge-Petruska scheme, characterized by the gap region length λ_G and by the axial period λ [4, 43]. As proved by well-established histological evidence, mineral particles are nucleated primarily inside the gap regions of the fibril, extending in a later stage into the overlap regions [4, 44, 45]. As a

result, the mineral phase is arranged within a water-protein-collagen (WPC) matrix, with a volume fraction in healthy cortical bone in the order of 40%, determining the peculiar tissue features in terms of stiffness and toughness. The shape of mature HA crystals is generally rather irregular, but many investigations showed that they are for most platelet-shaped [6, 44, 46].

On account of the spatial organization of bone nanoconstituents, MCFs are modelled as a composite material in which the reinforcement phase, represented by the HA platelets, is arranged in a staggered manner and embedded within a water-protein-collagen matrix, as shown in Fig. 3(b) [35, 45, 47]. By introducing a local reference system $\{\mathbf{e}_1, \mathbf{e}_2, \mathbf{e}_3\}$, with the $\mathbf{e}_3$-axis aligned along the MCF axis, the mineral platelets have been assumed as parallelepipedic, with linear dimensions along the $\mathbf{e}_1$, $\mathbf{e}_2$ and $\mathbf{e}_3$ axes equal to d_{HA}, b_{HA} and ℓ_{HA}, respectively. Symbols Δd_{HA} and Δb_{HA} respectively denote the along-the-width and along-the-depth gaps between two adjacent HA platelets.

The mineral phase is assumed to behave as an isotropic linearly-elastic material, characterized by an elastic stiffness tensor $\mathbb{C}_{\mathrm{HA}}$ dependent on Young's modulus E_{HA} and Poisson's ratio ν_{HA}. On the other hand, the WPC matrix for the MCFs has been regarded as a composite material made up by tropocollagen molecules, having volume fraction Φ'_c, embedded in a water-protein matrix (with volume fraction $\Phi'_{wp} = 1 - \Phi'_c$). The elasticity of the water-protein matrix is affected by hydrogen bonds linking the collagen molecules and by crosslinks provided by the NCPs [48]. Then again, since the big difference in stiffness between collagen and mineral phase, and due to their relative amount, the MCFs mechanical response is not affected by non-linear regimes characterizing unmineralized collagen and induced by sub-nanoscale mechanisms [16]. In fact, for typical values of mineral volume fraction, the influence of "toe" and "heel" regions characterizing the J-shaped stress-strain curve of unmineralized collagen fibrils tends to disappear [44, 45]. Accordingly, collagen comprising WPC matrix in MCFs is assumed to behave as an isotropic linearly-elastic material.

Equivalent properties of WPC matrix. Due to the geometrical arrangement of tropocollagen molecules, WPC composite can be described as an equivalent transversely-isotropic material, having $\mathbf{e}_3$ as the constitutive symmetry axis and the plane $(1, 2)$ as the isotropic plane. Let ph be the phase index, such that $ph \in \{wp, c\}$, where wp refers to the water-protein matrix and c to the collagen molecules, respectively. Moreover, let E_{ph}, ν_{ph}, G_{ph} and k_{ph} be the

Young's modulus, Poisson's ratio, shear modulus and bulk modulus of phase ph, respectively. Equivalent elastic constants in the isotropic plane have been obtained by following the modelling strategy proposed by Torquato [49] and applied by Nikolov and Raabe [48] for describing water-protein-collagen response in bone tissue at submicron scales. The longitudinal (i.e., along the $\mathbf{e}_3$ direction) equivalent elastic modulus and the corresponding Poisson's ratio are obtained by employing Hill's lower bounds for long-fiber composites under the condition that $G_c > G_{wp}$ [50]. Finally, the equivalent longitudinal shear modulus is computed by applying the rule of mixtures [51]. Thereby, the equivalent elastic constants of WPC matrix result in [48–50]:

$$G_{\mathrm{WPC},12} = G_{wp}\left[\frac{1 + k_{wp}\,\mu'\,\Phi'_c - F_\xi - F_\eta}{1 - (k_{wp} + 2G_{wp})\,\mu'\,\Phi'_c - F_\xi - F_\eta}\right] \tag{2}$$

$$k_{\mathrm{WPC},12} = k_{wp}\left[\frac{1 + G_{wp}\,\kappa'\,\Phi'_c - 2F_\xi}{1 - k_{wp}\,\kappa'\,\Phi'_c - 2F_\xi}\right] \tag{3}$$

$$E_{\mathrm{WPC},33} = \Phi'_{wp}E_{wp} + \Phi'_c E_c + \frac{4\Phi'_{wp}\Phi'_c(\nu_{wp} - \nu_c)^2}{\frac{\Phi'_{wp}}{k_c} + \frac{\Phi'_c}{k_{wp}} + \frac{1}{G_c}} \tag{4}$$

$$\nu_{\mathrm{WPC},31} = \Phi'_{wp}\nu_{wp} + \Phi'_c\nu_c + \frac{\Phi'_{wp}\Phi'_c(\nu_{wp} - \nu_c)\left(\frac{1}{k_{wp}} + \frac{1}{k_c}\right)}{\frac{\Phi'_{wp}}{k_c} + \frac{\Phi'_c}{k_{wp}} + \frac{1}{G_c}} \tag{5}$$

$$G_{\mathrm{WPC},13} = \left(\frac{\Phi'_{wp}}{G_{wp}} + \frac{\Phi'_c}{G_c}\right)^{-1} \tag{6}$$

where k_{wp} and k_c, in agreement with [48, 49], have the meaning of plane-strain bulk moduli (namely, are related to the three-dimensional bulk modulus K_{ph} of the phase ph by the relationship $k_{ph} = K_{ph} + G_{ph}/3$), and [49]:

$$F_\xi = k_{wp}\,G_{wp}\,\mu'\,\kappa'\,\Phi'_{wp}\,\xi \tag{7}$$

$$F_\eta = k_{wp}^2\,\mu'^2\,\Phi'_{wp}\,\eta \tag{8}$$

$$\kappa' = \frac{k_c - k_{wp}}{k_{wp}\,(k_c + G_{wp})} \tag{9}$$

$$\mu' = \frac{G_c - G_{wp}}{k_{wp}\,G_{wp} + (k_{wp} + 2G_{wp})\,G_c} \tag{10}$$

with ξ and η being dimensionless scalar parameters defined by threefold integrals depending on WPC microstructure [52, 53]. By assuming that the

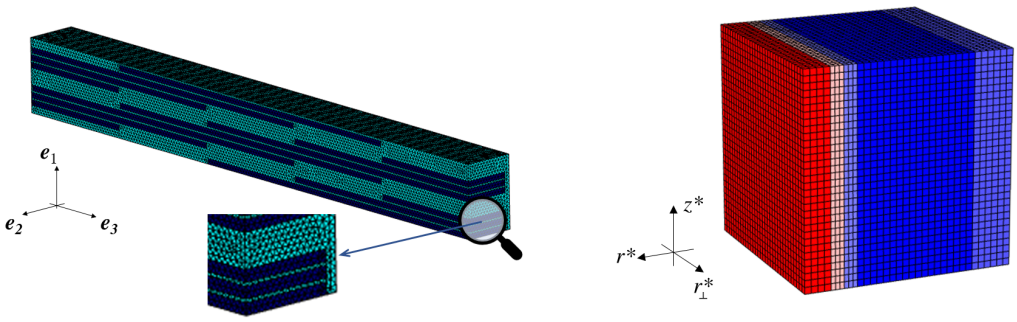

Figure 4: Computational domains associated to representative unit cells employed in the two-step numerical homogenization procedure to obtain the equivalent elastic properties of (a) MCFs and (b) lamellar tissue.

arrangement of collagen within WPC domain can be described as hexagonal arrays of cylinders, McPhedran and Milton [52], and Eischen and Torquato [53] furnished numerical solutions for parameters ξ, η for different values of collagen volume fractions. The equivalent stiffness tensor $\mathbb{C}_{\mathrm{WPC}}$ of WPC matrix is thereby completely determined.

Equivalent properties of MCFs. The MCFs equivalent elastic stiffness tensor $\mathbb{C}_{\mathrm{MCF}}$ is obtained as a result of a numerical homogenization procedure of the WPC-HA staggered composite previously described (see Fig. 3(b)). In detail, as illustrated in Fig 4(a), by defining the geometrical quantities $d_f = d_{\mathrm{HA}} + \Delta d_{\mathrm{HA}}$ and $b_f = b_{\mathrm{HA}} + \Delta b_{\mathrm{HA}}$, a Representative Unit Cell (RUC) having sides along the $\mathbf{e}_1$, $\mathbf{e}_2$ and $\mathbf{e}_3$ axes equal to $10d_f$, b_f and $2\ell_f$ in length, respectively, has been considered. In agreement with available histological and physical data, Table 1 lists the values of geometrical and constitutive parameters defining the nanoscale RUC employed to compute the elastic stiffness tensors $\mathbb{C}_{\mathrm{HA}}$ and $\mathbb{C}_{\mathrm{WPC}}$. In particular, the volume fraction of HA within the MCFs, also known as the degree of mineralization of cortical tissue, results in:

$$\Phi = \frac{\ell_{\mathrm{HA}}}{\ell_f} \cdot \frac{b_{\mathrm{HA}}}{b_f} \cdot \frac{d_{\mathrm{HA}}}{d_f} \tag{11}$$

As a consequence, by denoting with Φ_{wp} and Φ_c the volume fractions of water-protein and collagen within MCFs, the condition $\Phi_{wp} + \Phi_c + \Phi = 1$ has to be satisfied. The volume fractions Φ'_{wp} and Φ'_c of water-protein and

Table 1: Vaules of the nano-scale model parameters employed in numerical simulations.

Nanoscale (MCFs)			
Parameter	**Symbol**	**Value**	**References**
Degree of mineralization	Φ [%]	40	[45, 54]
Water-protein volume fraction	Φ_{wp} [%]	15	[55]
Tropocollagen molecules undeformed length	ℓ_c [nm]	300	[43, 44]
Axial period	λ [nm]	67	[4, 43]
Gap region length	λ_G [nm]	40	[4, 43]
HA platelets width	d_{HA} [nm]	3	[4, 11, 44]
HA platelets depth	b_{HA} [nm]	25	[4, 11, 44]
Along-the-width spacing between HA platelets	Δd_{HA} [nm]	1	[47, 56]
Along-the-depth spacing between HA platelets	Δb_{HA} [nm]	3	[47, 56]
Collagen Young's modulus	E_c [GPa]	1	[16, 57–59]
Collagen Poisson's ratio	ν_c [−]	0.28	[55, 60]
Water-protein Young's modulus	E_{wp} [GPa]	0.40	[48, 55]
Water-protein Poisson's ratio	ν_{wp} [−]	0.47	[48, 55]
HA platelets Young's modulus	E_{HA} [GPa]	114	[61, 62]
HA platelets Young's modulus	ν_{HA} [−]	0.27	[61]
Parameter ξ	ξ [−]	0.037	[52]
Parameter η	η [−]	0.471	[53]

collagen within the WCP composite matrix only, employed in Eqs. (2)-(8), can therefore be evaluated as:

$$\Phi'_{wp} = \frac{\Phi_{wp}}{\Phi_{wp} + \Phi_c} \tag{12a}$$

$$\Phi'_{c} = \frac{\Phi_{c}}{\Phi_{wp} + \Phi_c} \tag{12b}$$

By employing data in Table 1, and by noting that $\ell_f = \ell_c + \lambda_G$, for a given value of Φ the corresponding crystal length ℓ_{HA} can be derived by Eq. (11). In particular, for $\Phi = 0.40$, the corresponding ℓ_{HA} value lies within the commonly observed range of variability for healthy cortical tissue reported by several authors [45, 54, 56, 63].

As a result of a preliminary convergence analysis, the RUC has been discretized through second-order displacement-based tetrahedral elements with

an average size $h_{\mathrm{MCF}} = d_{HA}/3$ (see Fig. 4(a)). Periodic Boundary Conditions (PBC) have been enforced at the RUC boundary [64, 65]. The resulting homogenized stiffness tensor $\mathbb{C}_{\mathrm{MCF}}$ can be represented with respect to the local basis $\{\mathbf{e}_1, \mathbf{e}_2, \mathbf{e}_3\}$ (see Fig. 4(a)) and in Voigt notation as (in [GPa]):

$$[\mathbb{C}_{\mathrm{MCF}}] = \begin{bmatrix} 3.854 & 1.493 & 1.775 & 0 & 0.004 & 0 \\ 1.493 & 11.343 & 3.106 & 0.002 & -0.045 & 0 \\ 1.775 & 3.106 & 37.189 & 0.006 & -0.893 & 0 \\ 0 & 0.002 & 0.006 & 2.337 & 0 & -0.045 \\ 0.004 & -0.045 & -0.893 & 0 & 0.691 & 0 \\ 0 & 0 & 0 & -0.045 & 0 & 0.813 \end{bmatrix} \tag{13}$$

highlighting a quasi-monoclinic equivalent constitutive symmetry for MCF.

2.2.2. Microscale: single lamella

As confirmed by histological evidence, the single lamellar unit can be assumed to be constituted by $N_s = 5$ adjacent sublayers (or sublamellae). In turn, each sublamella is made up by bundles of MCFs roughly parallel to each other, but having different orientations in the different sublayers, giving rise to the so-called rotated-twisted-plywood structure [8, 9]. The MCFs orientation in the j-th sublayer ($j = 1, \ldots, N_s$) of the i-th lamella ($i = 1, \ldots, N$), with respect to the osteon long axis z, can be uniquely characterized by two angles χ_j^i and ψ_j^i [8, 66]. In particular, as sketched in Figs. 3(c) and 3(d), by introducing a local orthogonal reference system $(r^*, r_\perp^*, z^*)$, r^* and $r_\perp^*$ being the local radial and circumferential direction at the angle $\theta = \theta^*$, respectively, χ_j^i is the plywood angle (namely, the rotation angle of the MCFs around r^*), and ψ_j^i is the rotation angle around $r_\perp^*$ [6].

If δ_j^i denotes the thickness of the j-th sublayer within the i-th osteonic lamella, the thickness of this latter straight results in:

$$\delta_{lam}^i = \sum_{j=1}^{N_s} \delta_j^i \tag{14}$$

The elastic stiffness tensor $\mathbb{C}_j^i$ of the j-th sublayer within the i-th lamella in the global cylindrical reference system is obtained by transforming the representation of $\mathbb{C}_{\mathrm{MCF}}$ passing from the local reference basis $\{\mathbf{e}_1, \mathbf{e}_2, \mathbf{e}_3\}$ to the (r, θ, z) coordinate system. In detail, by adopting Voigt notation, it results [51]:

Table 2: Values of the micro-scale model parameters employed in numerical simulations.

Microscale (Single lamellae)							
Parameter	**Symbol**	**Value(s)**					**References**
Number of sublamellae	N_s	5					[9, 47]
Sublamella index	j	1	2	3	4	5	
MCFs plywood angle	χ_j [°]	0	30	60	90	120	[8, 67]
MCFs rotation angle	ψ_j [°]	0	0	0	70	30	[8, 67]
Sublamella thickness	δ_j [µm]	0.6	1.8	0.2	0.2	0.4	[66]
Lamella thickness	δ_{lam} [µm]	3.2					Eq. (14)

$$[\mathbb{C}^i_j] = [\mathbb{T}_j]\,[\mathbb{C}_{\text{MCF}}]\,[\mathbb{D}_j]^{-1} \tag{15}$$

where the transformation matrices $[\mathbb{T}_j]$ and $[\mathbb{D}_j]$ depend on angles χ^i_j and ψ^i_j and are reported in the Appendix. Following well-established evidence [6, 8, 66], sublamellae are assumed to be characterized by the same sequence of values for angles χ^i_j and ψ^i_j, and for the thickness δ^i_j in each lamella, namely $\chi^i_j = \chi_j$, $\psi^i_j = \psi_j$, $\delta^i_j = \delta_j$, and $\delta^i_{lam} = \delta_{lam}$ for each $i = 1, \ldots, N$.

A further numerical homogenization step allows to reduce the lamellar tissue to an equivalent locally-homogeneous linearly-elastic material, described by the fourth-order (undamaged) elastic stiffness tensor $\mathbb{C}^i_{lam}$. As a consequence of previous positions, it results $\mathbb{C}^i_{lam} = \mathbb{C}_{lam}$ for each $i = 1, \ldots, N$. By disregarding any curvature effect, the equivalent elastic stiffness tensor $\mathbb{C}_{lam}$ has been computed by employing a cubic RUC with an edge size equal to δ_{lam} in length. All the values of both structural and constitutive modelling parameters at the microscale are reported in Table 2.

As a result of a preliminary convergence analysis, a structured and uniform computational mesh, consisting in second-order brick elements and characterized by the mesh size $h_{lam} = \min_j \delta_j/3$, has been adopted (see Fig. 4(b)). Even in this case, PBC have been enforced at the RUC boundaries. The resulting (undamaged) lamellar stiffness tensor $\mathbb{C}_{lam}$ can be represented with respect to the cylindrical coordinate system (r, θ, z) and in Voigt notation as (in [GPa]):

$$[\mathbb{C}_{lam}] = \begin{bmatrix} 6.747 & 2.517 & 2.545 & 0.137 & -1.000 & -0.115 \\ 2.517 & 31.979 & 4.474 & -1.205 & -0.226 & -0.290 \\ 2.545 & 4.474 & 12.095 & -0.009 & -0.349 & 0.012 \\ 0.137 & -1.205 & -0.009 & 4.201 & -0.067 & -0.479 \\ -1.000 & -0.226 & -0.349 & -0.067 & 1.748 & 0.083 \\ -0.115 & -0.290 & 0.012 & -0.479 & 0.083 & 2.238 \end{bmatrix} \tag{16}$$

highlighting a fully-anisotropic equivalent constitutive symmetry.

2.2.3. Sub-macroscale: interlamellar interphases

As previously described, there exists a very thin material region between two subsequent lamellae, characterized by low stiffness level and known as interlamellar phase [68]. As stated by Rho et al. [4], the real composition of the interlamellar zones has still to be fully elucidated, but it seems that they result particularly rich in NCPs (primarily osteocalcin and osteopontin) and randomly-oriented collagen molecules [7, 69]. Nonetheless, such regions appear to have significant contributions on the mechanical behaviour of single osteons [68].

As a first approximation, due to the lack of information, interlamellar phases are assumed to be homogeneous and described by an isotropic linearly-elastic constitutive response. As such, the corresponding (undamaged) fourth-order elastic stiffness tensor $\mathbb{C}_{int}$ is fully characterized by the Young's modulus E_{int} and the Poisson's ratio ν_{int}.

Following an approach similar to the one adopted in [70], the interlamellar phases are treated as soft elastic interfaces $\mathcal{I}_i$ joining two subsequent osteonic lamellae. Accordingly, by denoting with $\hat{\mathbf{n}}_{int}^{(i)}$ the unit vector normal to $\mathcal{I}_i$, and under the plane-strain assumption, the second-order interface stiffness tensor $\mathbb{K}_{int}^{(i)}$ associated to $\mathbb{C}_{int}$ is obtained via a through-the-thickness first-order asymptotic expansion as [71]:

$$\mathbb{K}_{int}^{(i)} = K_n^{(i)} \hat{\mathbf{n}}_{int}^{(i)} \otimes \hat{\mathbf{n}}_{int}^{(i)} + K_t^{(i)} (\mathbb{I} - \hat{\mathbf{n}}_{int}^{(i)} \otimes \hat{\mathbf{n}}_{int}^{(i)}) \tag{17}$$

where $\mathbb{I}$ is the second-order identity tensor and $K_n^{(i)}$, $K_t^{(i)}$ are normal and tangential stiffness per unit surface, respectively equal to:

$$K_n^{(i)} = \frac{E_{int}\,(1-\nu_{int})}{(1+\nu_{int})\,(1-2\nu_{int})\,\delta_{int}^{(i)}} \tag{18a}$$

$$K_t^{(i)} = \frac{E_{int}}{2\,(1+\nu_{int})\,\delta_{int}^{(i)}} \tag{18b}$$

where $\delta_{int}^{(i)}$ is the thickness of the i-th interlamellar phase.

2.3. Failure criteria and damage law

The mechanical behaviour of a single osteon up to the failure state is described by accounting for the progressive loss of structural integrity due to loading-induced nucleation and propagation of microcracks. All osteonic tissues at the sub-macroscale level are considered as perfectly brittle materials, namely characterized by the absence of any local damage accumulation prior to local failure. In the framework of a stress-based damage description, failure in a material point $P \in \Omega$ is said to occur when:

$$F(P, \boldsymbol{\sigma}) = 1 \tag{19}$$

where $F(P, \boldsymbol{\sigma})$ depends on the failure criterion in P and on the local stress state $\boldsymbol{\sigma}(P)$.

Since the osteon has been herein conceived as a multi-layered composite material, both interlaminar and intralaminar failure modes have been considered. The former, occurring in correspondence of the interlamellar interfaces, is caused by delamination between two adjacent lamellae, whereas the latter occurs in the lamellar bulk tissue. As such, function F is specialized depending on the material point position $P \in \Omega$ as:

$$F(P, \boldsymbol{\sigma}) = \begin{cases} F_{lam}(\boldsymbol{\sigma}) & \text{if } P \in \mathring{\mathcal{L}} \\ F_{int}(\boldsymbol{\sigma}) & \text{if } P \in \mathcal{I} \end{cases} \tag{20}$$

In detail:

- For the interlaminar failure mode ($P \in \mathcal{I}$), and in agreement with [35], the quadratic Brewer-Lagacé criterion is adopted. In this case only σ_{rr}, $\sigma_{r\theta}$ and σ_{rz} stress components (with respect to the cylindrical reference system introduced in Fig. 2) contribute to failure and function F_{int} reads as [72]:

$$F_{int}(\boldsymbol{\sigma}) = \left(\frac{\langle \sigma_{rr} \rangle}{S_{rr}}\right)^2 + \left(\frac{\sigma_{r\theta}}{S_{r\theta}}\right)^2 + \left(\frac{\sigma_{rz}}{S_{rz}}\right)^2 \tag{21}$$

where $\langle \sigma_{rr} \rangle = \max\{0, \sigma_{rr}\}$ denotes the positive part of σ_{rr}, and S_{rr} and $S_{r\theta}$, S_{rz} are tensile and shear strength parameters of the interfaces. Note that the positive part of σ_{rr} plays the role of preventing closing mechanisms of interfacial microcracks under local radial compressive states [35].

- For the intralaminar failure mode ($P \in \mathring{\mathcal{L}}$), two different criteria are alternatively considered for the sake of comparison. The first one is the maximum principal stress criterion, corresponding to:

$$F_{lam}(\boldsymbol{\sigma}) = \max\{F^+, F^-\} \tag{22}$$

where:

$$\begin{aligned} F^+ &= \frac{\max\{0, \sigma_1, \sigma_2, \sigma_3\}}{S^+_{lam}} \\ F^- &= -\frac{\min\{0, \sigma_1, \sigma_2, \sigma_3\}}{S^-_{lam}} \end{aligned} \tag{23}$$

with σ_i $(i = 1, 2, 3)$ denoting the principal stress components and S^+_{lam} (resp., S^-_{lam}) being a positive lamellar strength measure in tension (resp., in compression).

The second one is the Von Mises criterion. Accordingly, by denoting with $\boldsymbol{s}$ the deviatoric part of $\boldsymbol{\sigma}$, function F_{lam} reads as:

$$F_{lam}(\boldsymbol{\sigma}) = \sqrt{\frac{3}{2}\mathrm{tr}(\boldsymbol{s}^2)} \Big/ S_{lam} \tag{24}$$

S_{lam} being a strength parameter for the lamellar bulk tissue.

It is noted that the experimental data provided by Ascenzi et al. [38, 40] allow to deduce a clear indication on S^+_{lam}, whereas, to the best of the authors' knowledge, no data are available for S^-_{lam}. Nevertheless, the experimental tests conducted by Ascenzi et al. [40, 73] on single fully calcified osteons both in tension and in compression seem to suggest that lamellar strength under compressive states is in the same order of magnitude of the tensile one. Accordingly, in the following it is assumed $S_{lam} = S^+_{lam} = S^-_{lam}$.

In accordance with the isotropic continuum damage mechanics theory, when the failure condition is locally detected, material stiffness of phase h (with $h \in \{int,\, lam\}$) is degraded by rescaling all the components of the local constitutive tensor via a scalar damage variable D_h. To ensure irreversibility conditions, thus making the damage model thermodynamically consistent, a scalar parameter for the phase h, κ_h, is introduced to record the maximum value of F_h ever reached in P during the loading history:

$$\kappa_h = \max_{\text{history}} \{F_h(\boldsymbol{\sigma})\} \qquad h \in \{int,\, lam\} \tag{25}$$

As a consequence, the local constitutive tensor results in:

$$\mathbb{C}(P, \kappa_{lam}, \kappa_{int}) = \begin{cases} \mathbb{C}_{lam}\big[1 - D_{lam}(\kappa_{lam})\big] & \text{if } P \in \mathring{\mathcal{L}} \\ \mathbb{C}_{int}\big[1 - D_{int}(\kappa_{int})\big] & \text{if } P \in \mathcal{I} \end{cases} \tag{26}$$

Owing to the bone tissue brittleness, D_h is assumed to obey the following degradation rule:

$$D_h(\kappa_h) = \begin{cases} 0 & \text{if } \kappa_h < 1 \\ D_{cr,h} & \text{if } \kappa_h = 1 \end{cases} \qquad h \in \{int,\, lam\} \tag{27}$$

$D_{cr,h} < 1$ being a critical value of the damage variable D_h. By discriminating local tensile and compressive states, $D_{cr,h}$ has been assumed equal to:

$$D_{cr,h} = \begin{cases} D^{+}_{cr,h} & \text{if } I_{1,h} \geq 0 \\ D^{-}_{cr,h} & \text{if } I_{1,h} < 0 \end{cases} \tag{28}$$

where $I_{1,lam} = \mathrm{tr}(\boldsymbol{\sigma})$ denotes the first stress invariant and $I_{1,int} = \sigma_{rr}$.

3. Numerical treatment

The developed multiscale elasto-damage approach has been implemented in a numerical framework based on a FE formulation. It has been validated by replicating three distinct loading scenarios corresponding to three different mechanical experiments performed on single osteons by Ascenzi and coworkers [39–41]. Characteristic dimensions at the sub-macroscale level of both osteonal geometry and loading zones replicate the ones actually adopted in the experimental benchmarks. In particular, by assuming that $\delta^{(i)}_{int} = \delta_{int}$ for

Table 3: Vaules of the model parameters at the osteon level employed in numerical simulations.

Sub-macroscale (Single osteon)			
Parameter	**Symbol**	**Value(s)**	**References**
Osteon inner diameter	D_H [µm]	40.0	[39–41]
Osteon outer diameter	D_O [µm]	210.4	[39–41]
Osteon length	L [µm]	500.0	[39–41]
Number of lamellae	N [−]	26	Eq. (29)
Lacunae dimensions	a [µm]	22	[1, 42]
	b [µm]	9	[1, 42]
	c [µm]	4	[1, 42]
Lacunae volume fraction	f_l [%]	2.1	[1]
Number of lacunae	N_l [−]	104	Eq. (1)
Interlamellar interface thickness	δ_{int} [µm]	0.08	[69]
Interlamellar interface Young's modulus	E_{int} [GPa]	3	[68]
Interlamellar interface Poisson's ratio	ν_{int} [−]	0.3	[68]
Interfaces radial strength	S_{rr} [MPa]	50	[35, 74, 75]
Interface circumferential shear strength	$S_{r\theta}$ [MPa]	70	[35, 74, 75]
Interface axial shear strength	S_{rz} [MPa]	70	[74, 75]
Lamellar strength	S_{lam} [MPa]	160	[76]
Critical damage in tension	D_{cr}^{+} [−]	0.99	[31]
Critical damage in compression	D_{cr}^{-} [−]	0.50	[31]
Dimensions of Σ_s'' (B-test)	h_{zs} [µm]	50	[39]
	$h_{\theta s}$ µm]	20	[39]
Dimensions of Σ_l'' (B-test)	h_{zl} [µm]	40	[39]
	$h_{\theta l}$ µm]	125	[39]

each $i = 1, \ldots, N-1$, the diameters D_O and D_H are related to the number of lamellae N through the following relationship:

$$\frac{D_O - D_H}{2} = N\,\delta_{lam} + (N-1)\,\delta_{int} \tag{29}$$

Therefore, for a given D_H, the number N of lamellae is chosen as an integer number such that the osteon outer diameter D_O, computed through Eq. (29), lies in the range of osteonal samples employed in the experiments. Table 3 lists the values of all geometrical and material parameters characterizing the single-osteon computational models. Such values have been consistently selected from ranges reported in the mentioned references. In particular,

as extensively discussed in the foregoing, the highest indeterminacy concerns the mechanical properties of interlamellar interfaces and the lamellar strength parameter S_{lam}, which will be addressed in future works.

Numerical procedures have been implemented through customized codes in Matlab environment (Matlab v. R2018a, MathWorks, MA, USA) integrated within the FE solver Comsol Multiphysics (Comsol with Matlab, v.5.4 COMSOL, Stockholm, Sweden). Second-order displacement-based tetrahedral elements have been employed to discretize the lamellar regions and three-dimensional spring elements are considered for discretizing interlamellar interfaces. The average mesh element size in lamellar regions has been set equal to $h = \delta_{lam}/2$ as a result of a preliminary convergence analysis ensuring mesh-independent results, and as discussed in Section 4.1.

3.1. Boundary conditions

To validate the proposed model, the osteonal mechanical response has been investigated addressing: a tensile test (denoted as T-test) [40], a torsion test (Θ-test) [41], and a three-point bending test (B-test) [39]. To faithfully mimic the experiments, proper boundary conditions have been enforced in each case. Moreover, with the aim of reducing the demanding computational cost of numerical simulations, and due to the geometrical and constitutive symmetry of the osteonal structure, a specific quarter of the domain Ω has been modelled, depending on the particular loading condition addressed. In detail, by referring to Fig. 5 and by recalling notation introduced in Sec. 2.1, the following assumptions have been made.

- T-test: the computational domain is defined by referring to a full-length quarter $\Omega' \subset \Omega$. In this case, $\Sigma_p \equiv \Sigma'_L$, $\Sigma_u \equiv \Sigma'_{r1} \cup \Sigma'_{r2} \cup \Sigma'_0$, and the following boundary conditions are enforced:

$$\mathbf{u} = \mathbf{0} \qquad \text{on } \Sigma'_0 \tag{30}$$

$$\mathbf{u} \cdot \hat{\mathbf{n}} = 0 \qquad \text{on } \Sigma'_{r1} \cup \Sigma'_{r2} \tag{31}$$

$$\mathbf{p} = p_T \, \hat{\mathbf{z}} \qquad \text{on } \Sigma'_L \tag{32}$$

with $\hat{\mathbf{n}}$ being the outward-pointing normal unit vector to $\partial\Omega'$, the relationship $\mathbf{u} \cdot \hat{\mathbf{n}} = 0$ representing symmetry conditions on $\Sigma'_{r1} \cup \Sigma'_{r2}$, and p_T (> 0) denoting the uniform distribution of the tensile loading per unit surface applied on Σ'_L.

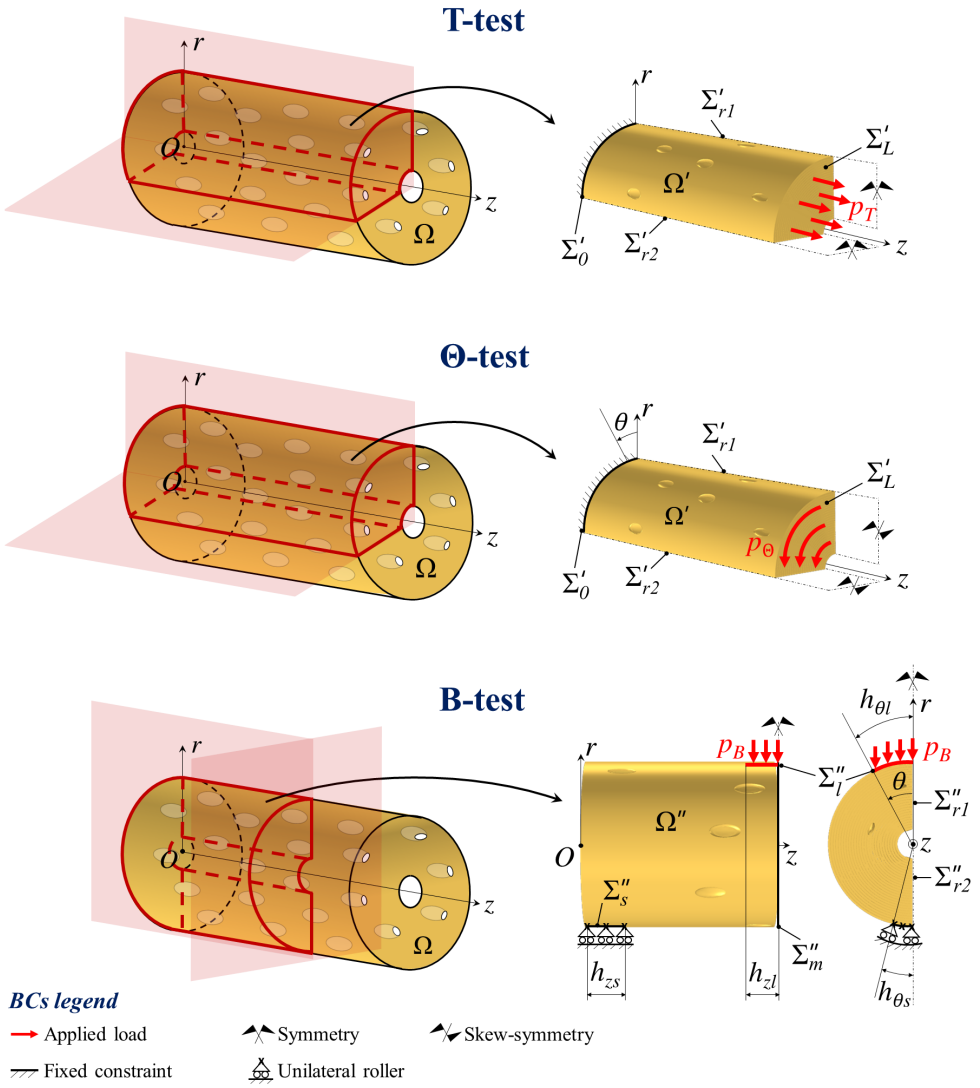

Figure 5: Applied boundary conditions for the three investigated loading scenarios. T-test: tension test; Θ-test: torsion test; B-test: bending test.

- Θ-test: the computational domain is defined by referring again to the full-length quarter $\Omega' \subset \Omega$ addressed in the T-test. In this case, $\Sigma_p \equiv \Sigma'_L$, $\Sigma_u \equiv \Sigma'_{r1} \cup \Sigma'_{r2} \cup \Sigma'_0$, and the following boundary conditions are enforced:

$$\mathbf{u} = \mathbf{0} \qquad \text{on } \Sigma'_0 \tag{33}$$

$$\mathbf{u} - (\mathbf{u} \cdot \hat{\mathbf{n}})\hat{\mathbf{n}} = \mathbf{0} \qquad \text{on } \Sigma'_{r1} \cup \Sigma'_{r2} \tag{34}$$

$$\mathbf{p} = p_\Theta(r)\, \hat{\boldsymbol{\theta}} \qquad \text{on } \Sigma'_L \tag{35}$$

where relationship in Eq. (34) represents skew-symmetry conditions on $\Sigma'_{r1} \cup \Sigma'_{r2}$, and $p_\Theta(r)$ (> 0) is the distribution of the circumferential loading per unit surface applied on Σ'_L, assumed equal to:

$$p_\Theta(r) = \frac{T}{J} r \qquad \text{with } J = \frac{\pi}{32}\left(D_O^4 - D_H^4\right) \tag{36}$$

where T is the resultant external torque associated to the experimental conditions.

- B-test: the computational domain is defined by referring to the half-length region $\Omega'' \subset \Omega$ shown in Fig. 5. In this case, $\Sigma_p \equiv \Sigma''_l$, $\Sigma_u \equiv \Sigma''_{r1} \cup \Sigma''_{r2} \cup \Sigma''_m \cup \Sigma''_s$, and the following boundary conditions are enforced:

$$\mathbf{u} \cdot \hat{\mathbf{n}} \leq 0 \qquad \text{on } \Sigma''_s \tag{37}$$

$$\mathbf{u} \cdot \hat{\mathbf{n}} = 0 \qquad \text{on } \Sigma''_{r1} \cup \Sigma''_{r2} \cup \Sigma''_m \tag{38}$$

$$\mathbf{p} = -(p_B \cos\theta)\, \hat{\mathbf{r}} + (p_B \sin\theta)\, \hat{\boldsymbol{\theta}} \qquad \text{on } \Sigma''_l \tag{39}$$

where the unilateral frictionless constraint $\mathbf{u} \cdot \hat{\mathbf{n}} \leq 0$ on Σ''_s models the simple support zones adopted in the experiments. Moreover, relationship in Eq. (38) enforces symmetry conditions on $\Sigma''_{r1} \cup \Sigma''_{r2} \cup \Sigma''_m$ and p_B (> 0) is the uniform distribution of the vertical loading per unit surface applied on Σ''_l and equal to:

$$p_B = \frac{F}{4|\Sigma''_l|} \tag{40}$$

with F being the resultant external force associated to the experimental conditions, and $|\Sigma''_l|$ is the area of the loaded region in the computational model. The boundary regions Σ''_s and Σ''_l are defined in agreement with the dimensional data furnished in [39], as summarized in Table 3.

3.2. Energy-based numerical regularization

Damage-based modelling approaches lead to mesh-sensitive results due to the phenomenon of strain localization upon mesh refinements. Objective results can be obtained if a suitable regularization technique is envisaged in the model [77]. A proper regularization technique has to account for a material characteristic length ℓ related to the internal heterogeneity and depending on the bandwith of the strain localization zones. For brittle materials this latter can be considered as a characteristic constitutive property of the material [78]. In this paper, following the approach proposed in [78], a regularization method based on a mesh-related local modification of material properties has been adopted. In particular, the experimental-based values of the ultimate strength parameters S_α (with $\alpha \in \{rr,\, r\theta,\, rz,\, lam\}$) are corrected under the constraint that the dissipated energy per unit crack surface U_d equals the corresponding energy in the discretized model.

As proved in [31], for the damage law given by Eq. (27), U_d is characterized by a quadratic dependence with respect to the ultimate parameter S_α, namely $U_d = O(\ell\, S_\alpha^2)$. As a consequence, the experimentally-obtained ultimate parameters S_α are replaced, in numerical applications and for each mesh element, by the corresponding corrected values:

$$S_{\alpha,\,\mathrm{FE}} = \sqrt{\frac{\ell}{h_e}}\, S_\alpha \qquad \alpha \in \{rr,\, r\theta,\, rz,\, lam\} \tag{41}$$

where h_e is the element characteristic dimension related to the local mesh size and defined as:

$$h_e = \begin{cases} \sqrt[3]{V_e} & \text{if } \alpha \in \{lam\} \\ \sqrt{A_n} & \text{if } \alpha \in \{rr,\, r\theta,\, rz\} \end{cases} \tag{42}$$

with V_e being the volume of a mesh element in lamellar bulk regions (namely, in $\mathcal{L}$) and A_n is a measure of the area associated to pair surface nodes connected by spring elements and modelling interlamellar interfaces $\mathcal{I}$. In particular, A_n is computed as the average area of the lying-on-$\mathcal{I}$ faces of elements concurring to the nodes [70, 79].

The material characteristic length ℓ is defined as depending on the osteonal substructures. In detail, the characteristic length $\ell_\mathcal{L}$ for the bulk regions is assumed equal to the minimum sublamellar thickness: $\ell_\mathcal{L} = \min_j \delta_j = 0.2\,\mu\mathrm{m}$; the characteristic length $\ell_\mathcal{I}$ for the interfaces is assumed equal to the thickness of the interlamellar zone: $\ell_\mathcal{I} = \delta_{int} = 0.08\,\mu\mathrm{m}$.

3.3. Iterative algorithm

The progressive damage within the osteonal structure is simulated by implementing a numerical iterative procedure, addressing a quasi-static load-controlled incremental approach. Equal loading increments have been applied in all previously-introduced loading scenarios, so that at the k-th computational step the corresponding loading value results in:

$$\text{in the T-test :} \qquad p_T^{(k)} = k p_0 \tag{43}$$

$$\text{in the } \Theta\text{-test :} \qquad p_\Theta^{(k)}(r) = k \frac{T_0}{J}\, r \tag{44}$$

$$\text{in the B-test :} \qquad p_B^{(k)} = k \frac{F_0}{4|\Sigma_l''|} \tag{45}$$

where p_0, T_0 and F_0 represent the loading increments in the T-, Θ- and B-test, respectively. Values of p_0, T_0 and F_0 adopted in the numerical simulations correspond to the ones actually employed in the benchmark experiments and are reported in Table 4, together with the corresponding deformation parameter evaluated for each loading scenario.

Starting from the discretized model of the osteon in the initial configuration, the undamaged stiffness tensors $\mathbb{C}_{lam}$ and $\mathbb{K}_{int}$ (see Eqs. (16) and (17)) are assigned to each lamellar or interface element, respectively. The linearly-elastic problem at k-th computational step is solved by disregarding volume forces and by applying one of the loading values defined by Eqs. (43)-(45) according to the addressed loading scenario. It is worth observing that when the B-test is considered, the presence of unilateral frictionless constraints needs – for each equilibrium step – a further sub-iteration phase in order

Table 4: Type and values of loading increments applied in the numerical simulations for the T-, Θ-, and B-tests, in agreement with data provided by [39–41]. The corresponding deformation parameter evaluated in each case is also reported.

Benchmark test	**Loading increment**	**Value**	**Deformation parameter**
T-test	p_0 [MPa]	5.0000	Elongation ε [%]
Θ-test	T_0 [$\times 10^{-5}$ N m]	1.4955	Angle of twist θ [$\times 10^{-2}$rad]
B-test	F_0 [N]	0.1226	Deflection Δ [µm]

to detect the portion of the boundary surface Σ_s'' (see Fig. 5) actually engaged in the unilateral contact. Once the solution of linearly-elastic problem is computed, the actual stress field $\boldsymbol{\sigma}$ is evaluated at each Gauss point and it is employed to compute functions F_{int}, F_{lam} described by Eqs. (21) and (24), respectively. If local failure occurs nowhere in Ω, namely conditions $F_{int}(\boldsymbol{\sigma}) < 1$ and $F_{lam}(\boldsymbol{\sigma}) < 1$ contemporary hold within the corresponding regions, the deformation parameter associated to the particular loading scenario (see Table 4) is computed. On the contrary, if local failure conditions are detected somewhere in the computational domain, the corresponding local material properties are degraded in agreement with Eq. (26). Moreover, the same computational step is iteratively repeated until further variations in the damage pattern are no longer revealed, thus ensuring equilibrium and compatibility. When this latter circumstance is attained, the subsequent computational step (namely, the $(k+1)$-th one) is performed. On the other hand, the complete failure is assumed to be reached at the k-th computational step if, after a fixed number of repetitions (herein assumed equal to 20), local damage continues to be detected.

4. Results and discussion

4.1. Preliminary convergence results

To validate the regularization technique described in Section 3.2, the osteonal mechanical response has been numerically investigated by using three different mesh refinements. In detail, in bulk lamellar regions an average element size equal to δ_{lam}, $\delta_{lam}/2$ and $\delta_{lam}/3$ has been adopted for defining rough, average and fine mesh, respectively. For the sake of conciseness, only numerical results relevant to the B-test and implementing the maximum principal stress criterion are reported below. Simulations addressing other loading scenarios and failure treatment showed similar responses.

Panel in Fig. 6 reports the numerically-predicted osteonal mechanical response in terms of force-deflection curve for the three mesh refinement levels, and up to the complete failure state. Proposed preliminary results clearly prove the effectiveness of the regularization approach presented in the foregoing. In particular, as a right balance between model accuracy and computational cost, the subsequent numerical analyses have been conducted by employing the average mesh refinement.

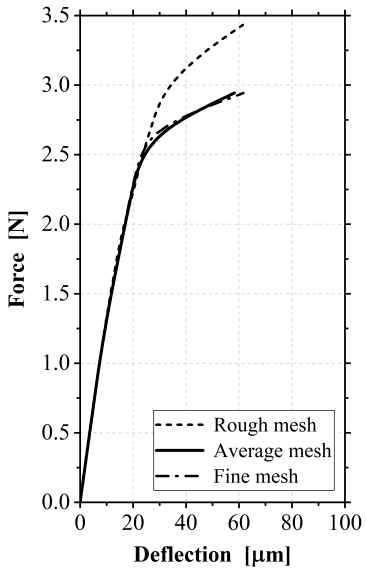

Figure 6: Mesh convergence analysis. Numerically-predicted osteonal mechanical behaviour in terms of force-deflection curve in the case of the B-test loading condition.

4.2. Osteon mechanical behaviour

In the following, obtained FE predictions of the osteon mechanical behaviour under the herein-considered loading conditions are illustrated and compared to the available experimental data [39–41]. For each loading scenario, numerical results are provided in terms of:

- response curves associated to applied load vs. the related deformation parameter (see Table 4);
- osteon modulus of elasticity (MOE), defined in the following;
- load (FL) and deformation (FD) values at the complete failure state;
- damage pattern, defined as the set of all elements which experienced interlaminar and/or intralaminar failure up to a given load step.

In line with the beam theory, and referring to the notation introduced in Table 4, numerically-predicted MOE values associated to T-, Θ-, and B-test, respectively, have been computed following the approach adopted by Ascenzi and coworkers [39–41]. In deatil:

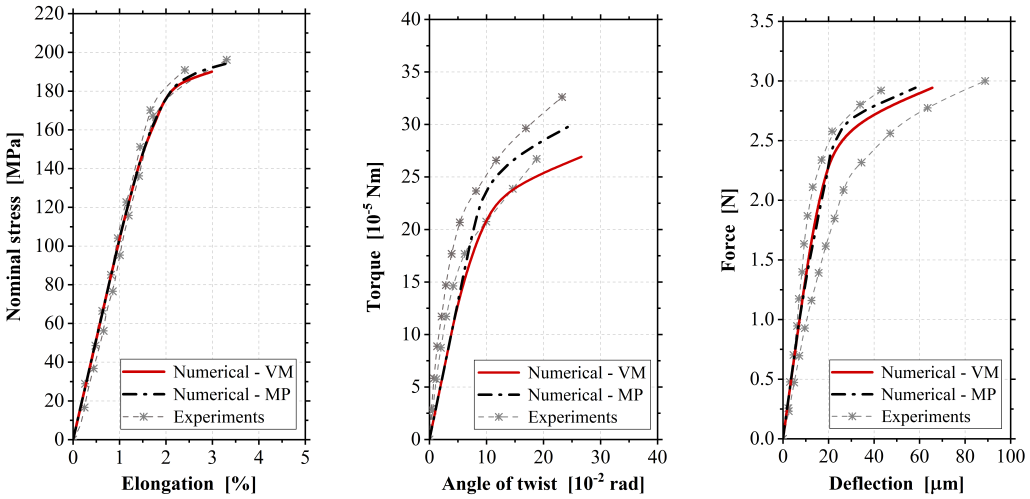

Figure 7: Mechanical response of a single osteon in different loading scenarios: (a) T-test, (b) Θ-test, (c) B-test. In each panel, the present numerical load-deformation curves are shown in comparison with benchmark experimental results (sources: [40], [41], [39] for the T-test, Θ-test and B-test, respectively). VM: Von Mises intralaminar strength criterion; MP: Maximum principal stress intralaminar criterion.

$$\text{in the T-test :} \qquad \text{MOE}_T = \frac{p_0}{\varepsilon^{(1)}} \tag{46}$$

$$\text{in the } \Theta\text{-test :} \qquad \text{MOE}_\Theta = \frac{T_0 L}{J\theta^{(1)}} \tag{47}$$

$$\text{in the B-test :} \qquad \text{MOE}_B = \frac{F_0 L^3}{48 I \Delta^{(1)}} \tag{48}$$

where superscript (1) identifies the value of the deformation parameters at the first numerical step, and $I = J/2$ is the moment of inertia along the radial direction.

Panels in Fig. 7 show the load-deformation curves obtained in the T-test (Fig. 7(a)), Θ-test (Fig. 7(b)) and B-test (Fig. 7(c)) by employing either the Von Mises or the maximum principal stress criterion for identifying intralaminar failure conditions. In the same panels, benchmark curves experienced in the corresponding mechanical tests [39–41] are also plotted. Table 5 reports predicted values of the osteon modulus of elasticity and failure parameters for each loading scenario, in comparison with the ones computed from the experimental curves.

Table 5: Values of the osteon modulus of elasticity (MOE), ultimate load (FL) and ultimate deformation parameter (FD) in T-, Θ- and B-test computed with present model and compared to benchmark data deduced from experimental curves [39–41, 80]. Experimental values by Ascenzi et al. [39–41] are given in terms of mean value and standard deviation. In the case of the Θ-test, reference is also made to average experimental results (reported in brackets) proposed by Bonfield and Li [80]. VM: Von Mises intralaminar strength criterion; MP: Maximum principal stress intralaminar criterion.

Test	**Parameters**	**Ref**	**Experimental values**		**Present model**	
					VM	MP
T-test	MOE_T [GPa]		10.84 ± 6.98		9.74	
	FL_T [MPa]	[40]	193.48 ± 31.97		190.00	195.00
	FD_T [%]		3.45 ± 0.38		2.99	3.42
Θ-test	MOE_Θ [GPa]		17.17 ± 3.35	(5.86)	6.90	
	FL_Θ [$\times 10^{-5}$ N m]	[41] ([80])	31.04 ± 2.77	(28.02)	26.92	29.91
	FD_Θ [$\times 10^{-2}$ rad]		18.09 ± 4.19	(30.21)	26.67	24.78
B-test	MOE_B [GPa]		3.32 ± 1.20		3.67	
	FL_B [N]	[39]	2.61 ± 0.38		2.94	2.94
	FD_B [µm]		66.01 ± 17.65		65.60	58.24

Present results clearly highlight that the osteon mechanical response up to the failure and associated to different loading scenarios is accurately predicted by the proposed approach. The comparative analysis with available experimental data proves soundness and consistency of numerical predictions, a better accuracy being attained when the maximum principal stress criterion is adopted for the intralaminar damage description. The mechanical response of the osteonal structure is well-described not only in the linear regime, but also when damage onset and evolution arise. In agreement with experimental evidence, the non-linear branches of curves in Fig. 7 indicate a rapid evolution of damage mechanisms under almost low loading increments, especially for T- and B-test. In the case of a twisting scenario, a more gradual damage evolution is successfully reproduced, corresponding to a larger load interval between damage initiation and failure.

As data summarized in Table 5 highlight, proposed numerical approach allows to quantitatively recover the osteon elastic modulus in the linear regime, as well as the failure state in terms of load and deformation levels. It should be noted that the little discrepancies between numerical and

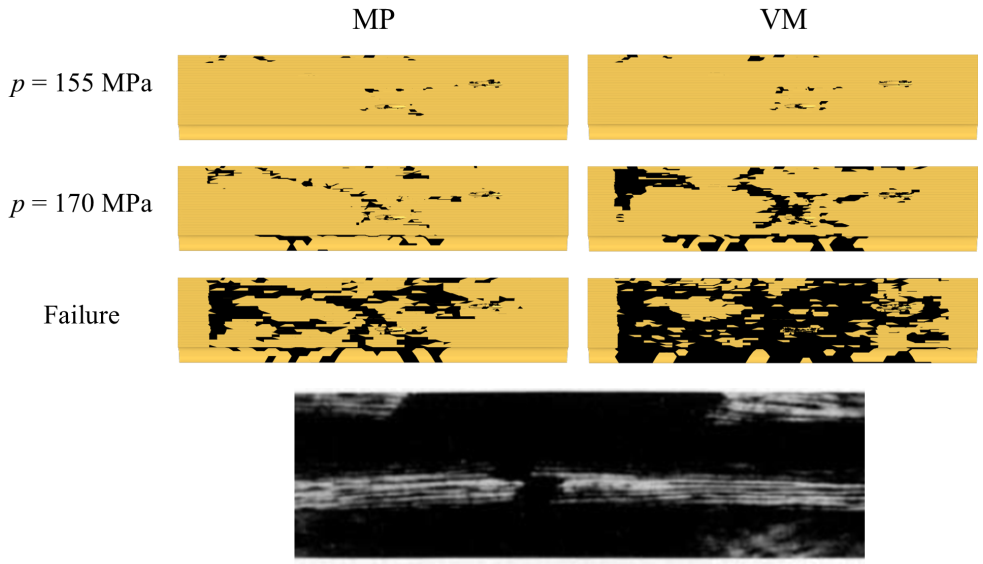

Figure 8: Damage patterns for a single osteon loaded in tension (T-test), under different levels of tensile loading per unit surface p in comparison with the experimental result (Courtesy from [40]). VM: Von Mises intralaminar strength criterion; MP: Maximum principal stress intralaminar criterion.

experimental data by Ascenzi et al. [41] and relevant to the Θ-test could be ascribed to possible spurious effects induced by the experimental equipment. In fact, as authors themselves declared, possible drawbacks affecting measurements might be associated to end effects produced by the jaws, low slenderness levels of adopted specimens, and possible occurrence of bending-torsional coupling induced by the end constraints. As a result, Θ-test experimental data provided in [41] do not perfectly agree with other available experimental findings, as those proposed by Bonfield and Li [80], the latter being very close to present numerical predictions.

Figures 8 to 10 depict the numerically-experienced damage patterns attained at three different load levels for the T-, Θ- and B-test, respectively. Exemplary fracture patterns obtained in the corresponding mechanical tests performed by Ascenzi and coworkers are also shown [39–41]. In detail, proposed results indicate some aspects affecting microdamage mechanisms. The onset of damage process, corresponding to the deviation from linearity in the curves of Fig. 7, is driven by the presence of lacunae, which thereby act as stress intensifiers. Accordingly, a proper prediction of damage initiation

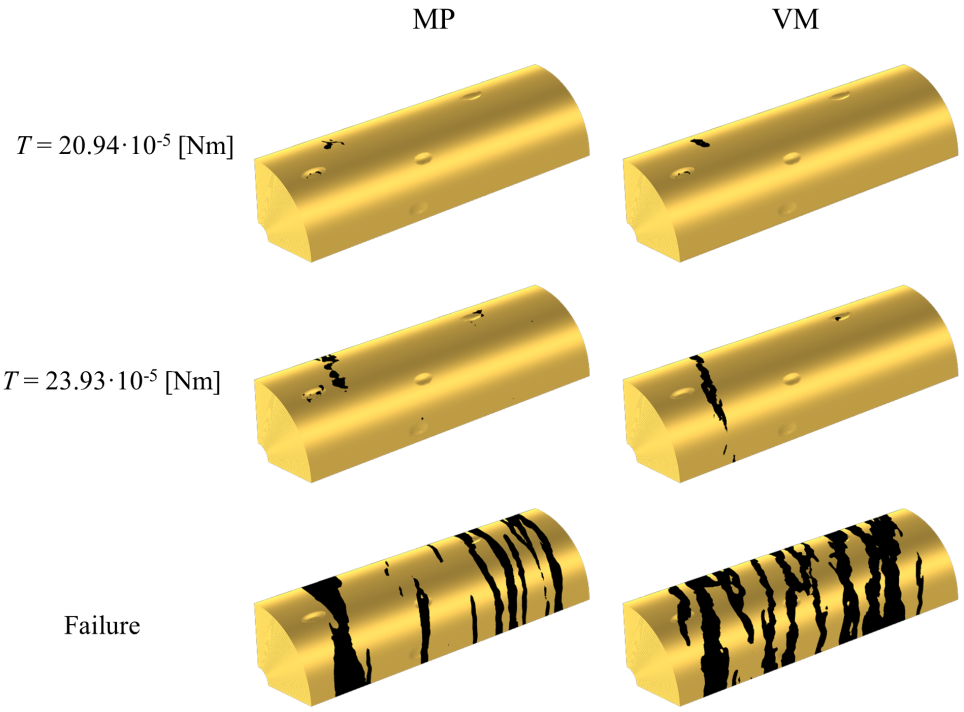

Figure 9: Damage patterns for a single osteon loaded in torsion (Θ-test), under different levels of external torque T in comparison with the experimental result (Courtesy from [41]). VM: Von Mises intralaminar strength criterion; MP: Maximum principal stress intralaminar criterion.

and propagation is strictly related to a suitable modelling of lacunar voids. Moreover, both the intralaminar and interlaminar failure mechanisms induce a significant effect in damage propagation. This latter is triggered by the occurrence of microcracks, and evolves as a consequence of microcrack coalescence, resulting in damage bands diffusing across the interlamellar regions. The set of damage bands exhibits an ordered arrangement strictly dependent on the loading type, in line with the experimental patterns observed by Ascenzi et al. [39–41]. In particular, the numerically-predicted damage pattern at the failure state in the case of a torsional load is characterized by a typical zebra-striped arrangement, with several multiple cracks evolving along quasi-circumferential directions (see Fig. 9). Such an evidence reproduces the experimental findings proposed in [41] and summarized in the Authors' statement "cracks affected osteons at a variety of levels". Finally, numerical

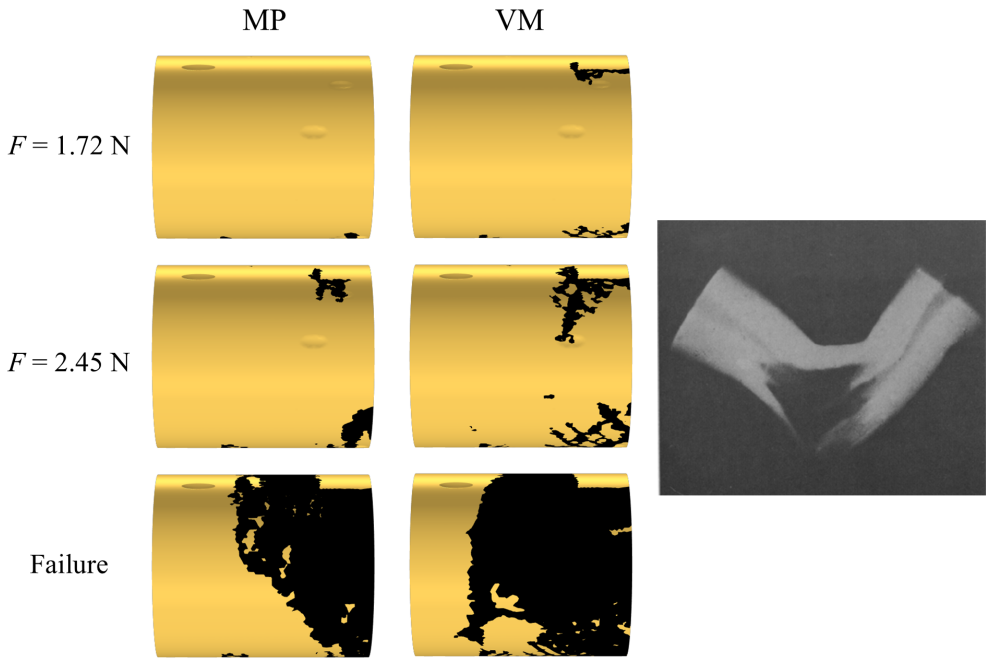

Figure 10: Damage patterns for a single osteon loaded in bending (B-test), under different levels of the resultant force F in comparison with the experimental result (Courtesy from [39]). VM: Von Mises intralaminar strength criterion; MP: Maximum principal stress intralaminar criterion.

simulations indicate that damage prediction is associated to a more ordered arrangement of bands in the case of maximum principal stress criterion rather than the Von Mises one.

4.3. Influence of the mineralization degree

Several evidence proved that biological factors such as ageing or the occurrence of diseases affect the structure and composition of bone tissue at each length scale, mainly causing a decrease in the degree of mineralization [1, 81]. As a result, bone stiffness reduces and the failure state tends to be characterized by higher deformation levels. This occurrence can be experienced both at the macroscale [1] and at the microscale (namely, at the osteon level) [40].

Present multiscale approach allows to straight account for biophysical alterations of bone tissue by varying model parameters with a clear histological meaning, thereby not in a phenomenological way. In detail, the alteration

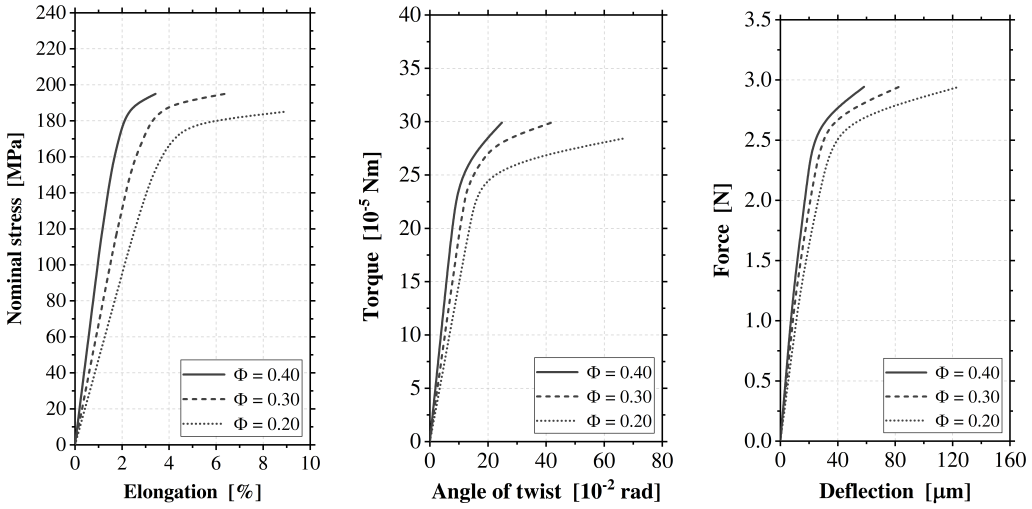

Figure 11: Effect of HA volume fraction at the nanoscale on the mechanical behaviour of a single osteon in different loading scenarios. (a) T-test, (b) Θ-test, (c) B-test.

of the bone mineralization degree can be straightforwardly reproduced by varying the parameter Φ introduced in Eq. (11). In the following, the MCFs equivalent properties have been referred to three different values of Φ: 0.20, 0.30, 0.40. The condition $\Phi = 0.40$ can be retained as representative of a perfectly healthy tissue (as previously highlighted), whereas the case $\Phi = 0.20$ corresponds to a low calcified tissue [1, 4]. The variability of Φ has been prescribed by varying the crystal edge length ℓ_{HA} (i.e., along the fibril axis, Fig. 3), since the values of the other HA-related dimensions lie in a very limited range [4, 47, 56].

For the three herein-considered loading scenarios, Fig. 11 reports the load-deformation curves of a single osteon for different values of Φ. It can be clearly seen that such a nanostructural parameter deeply affects the mechanical response of cortical bone at the microscale. In particular, moving from $\Phi = 0.40$ to $\Phi = 0.20$, the osteonal stiffness reduces by about 46%, 43% and 35% for the T-, Θ- and B-tests, respectively. The deviation from linearity is slightly dependent on the mineralization degree and in each case it occurs for load levels having the same order of magnitude with respect to the failure load values. In detail, when Φ reduces, failure states shift towards both slightly reduced failure loads and higher deformation levels.

Proposed results thereby confirm that cortical bone brittleness at the osteonal level increases with the mineralization degree, in agreement with available evidence (see e.g. [7, 82]). The slight dependence of the failure load on Φ can be related to the assumption, justified by the evidence provided in the available literature (see e.g. [40]), that local strength features are practically not affected by Φ.

As a further validation argument, the available experimental data relevant to tensile tests provided in [40] and associated to the case of "single osteons at lowest degree of calcification", are in full agreement with the case $\Phi = 0.20$ depicted in Fig. 11(a).

Numerically-experienced fracture mechanisms seem to be not significantly affected, in their onset and evolution, by the mineralization degree. Similar damage patterns under different values of Φ have been simulated and thereby they are not herein reported for the sake of compactness.

5. Concluding remarks

In this paper, the mechanical response of a single osteon under several loading scenarios has been investigated via a multiscale model, defined in agreement with histological evidence. All the introduced model parameters have a clear physical meaning and the corresponding values are straight identifiable by available experimental measurements. Reference is made to a typical osteonal geometry, based on a multi-layered arrangement of coaxial cylindrical lamellae, and accounting for some microstructural details, such as lacunar voids. Lamellar tissue has been described as an anisotropic material, whose equivalent constitutive response has been defined via a bottom-up multistep homogenization technique allowing to account for dominant nanoscale mechanisms. As a simplifying assumption, any fluid and viscous effects have been disregarded.

The influence of interlamellar regions is modelled by introducing equivalent soft interfaces, whose mechanical behaviour is consistently deduced via a through-the-thickness first order asymptotic expansion.

By assuming a brittle constitutive response of osteonal constituents, a progressive stress-driven damage approach has been conceived and implemented via a FE iterative procedure. Proposed model has been validated by reproducing available experimental set-ups [39–41], resulting in simulated mechanical response and damage mechanisms of the osteonal models in full agreement with the measurements on in-vitro samples.

The histologically-oriented conception of the proposed model allows to account for biophysical/biochemical alterations over multiple length scales, possibly induced by ageing or diseases, by straight varying – consistently with experimental evidence – values of specific model parameters. For instance, insights on the microscale mechanical response and failure mechanisms of bone structures, could be straightforwardly obtained by considering variations in collagen fibres orientations, thinning of lamellae, increasing in the lacunae volume fraction, alterations in morphology and shape of HA platelets, as well as changes in mineralization levels. As an exemplary application, the present refined multiscale strategy revealed to be able to successfully describe osteonal mechanical response by accounting for different mineralization levels of lamellar tissue.

Avoiding specific phenomenological descriptions, present model can be considered as suitable for being upscaled at the macroscopic organ level, in order to develop refined bone multiscale structural models, wherein subscale dominant mechanisms are accounted for and are directly related to measurable histological properties over multiple length scales. Moreover, present approach could be successfully exploited in an inverse-like numerical scheme, in order to give estimates of biophysical/biochemical features in tissue constituents, thereby contributing to overcoming the limitations of experimental approaches at low length scales [83–85]. It is worth pointing out that, to upscale the model up to the organ level, these perspective steps need to be coupled with refined experimental investigations and further modelling enhancements. In detail, present model may be improved by encompassing the trough-the-scales effects induced by less regular geometries and arrangements of the various cortical bone substructures. In addition, possible residual stress and prestress distributions or subscale inelastic effects, also related to the non-linear mechanics of collagen fibrils at the nanoscale, could further enhance the present constitutive description of lamellar tissue, particularly in cases where a low bone mineralization level is present. The constitutive description of interlamellar phases may be further refined by adopting chemical potential-based hyperelastic approaches (see e.g. [86]), as well as generalized energetic-based damage descriptions. As regards the modelling of the progressive failure process, useful information could be gleaned by comparing proposed results with the ones obtained through enhancements of damage theory (e.g., anisotropic description of damage, regularization through nonlocal models) and/or through the implementation of the phase-field approach for fracture. Finally, the interplay among several osteons (separated by ce-

ment lines, which are very weak interfaces) should be properly assessed, since it represents a key property which gives to cortical bone tissue its peculiar strength and toughness. There is indeed evidence that interfaces at upper hierarchical levels are able to make the sub-structures flaw tolerant [87, 88], provided that the interface properties satisfy suitable conditions, as pointed out in [89].

Acknowledgments

Part of this work was carried out within the support from the Italian National Group for Mathematical Physics GNFM-INdAM.

Elisabetta Monaldo acknowledges the financial support from the Italian Ministry of University and Research (MUR) under the Departments of Excellence grant L.232/2016.

Declaration of competing interest

Pierfrancesco Gaziano, Elisabetta Monaldo, Cristina Falcinelli and Giuseppe Vairo disclose any financial and personal relationships with other people or organizations that could inappropriately influence (bias) their work.

Appendix A. Matrix form of stress and strain transformation tensors

Let $\{Opqr\}$ and $\{Op'q'r'\}$ be two different orthogonal cartesian coordinate systems. The positions of axes p', q', r' with respect to axes p, q, r can be specified by means of three angles Θ_p, Θ_q, Θ_r, taken positive in the counterclockwise direction, representing the angles of consecutive rotations of primed system $\{Op'q'r'\}$ about the p, q, r axes, respectively. In present model, for the j-th sublayer constituting a given lamella, it results $\Theta_p = \chi_j$, $\Theta_q = 0$ and $\Theta_r = \psi_j$, respectively. Moreover, let symbols $c_h = \cos\Theta_h$, $s_h = \sin\Theta_h$ ($h \in \{p, q, r\}$) be introduced for the sake of compactness. Thereby, the matrix representations of tensors $\mathbb{T}_j$ and $\mathbb{D}_j$ employed in Eq. (15) result from [51]:

$$[\mathbb{T}_j] = [\mathbb{T}_j^p]\,[\mathbb{T}_j^q]\,[\mathbb{T}_j^r] \tag{A.1}$$

$$[\mathbb{D}_j] = [\mathbb{D}_j^p]\,[\mathbb{D}_j^q]\,[\mathbb{D}_j^r] \tag{A.2}$$

where:

$$[\mathbb{T}_j^p] = \begin{bmatrix} 1 & 0 & 0 & 0 & 0 & 0 \\ 0 & c_p^2 & s_p^2 & 2c_p s_p & 0 & 0 \\ 0 & s_p^2 & c_p^2 & -2c_p s_p & 0 & 0 \\ 0 & -c_p s_p & c_p s_p & c_p^2 - s_p^2 & 0 & 0 \\ 0 & 0 & 0 & 0 & c_p & -s_p \\ 0 & 0 & 0 & 0 & s_p & c_p \end{bmatrix} \tag{A.3}$$

$$[\mathbb{T}_j^q] = \begin{bmatrix} c_q^2 & 0 & s_q^2 & 0 & 2c_q s_q & 0 \\ 0 & 1 & 0 & 0 & 0 & 0 \\ s_q^2 & 0 & c_q^2 & 0 & -2c_q s_q & 0 \\ 0 & 0 & 0 & c_q & 0 & -s_q \\ -c_q s_q & 0 & c_q s_q & 0 & c_q^2 - s_q^2 & 0 \\ 0 & 0 & 0 & s_q & 0 & c_q \end{bmatrix} \tag{A.4}$$

$$[\mathbb{T}_j^r] = \begin{bmatrix} c_r^2 & s_r^2 & 0 & 0 & 0 & 2c_r s_r \\ s_r^2 & c_r^2 & 0 & 0 & 0 & -2c_r s_r \\ 0 & 0 & 1 & 0 & 0 & 0 \\ 0 & 0 & 0 & c_r & -s_r & 0 \\ 0 & 0 & 0 & s_r & c_r & 0 \\ -c_r s_r & c_r s_r & 0 & 0 & 0 & c_r^2 - s_r^2 \end{bmatrix} \tag{A.5}$$

$$[\mathbb{D}_j^p] = \begin{bmatrix} 1 & 0 & 0 & 0 & 0 & 0 \\ 0 & c_p^2 & s_p^2 & c_p s_p & 0 & 0 \\ 0 & s_p^2 & c_p^2 & -c_p s_p & 0 & 0 \\ 0 & -2c_p s_p & 2c_p s_p & c_p^2 - s_p^2 & 0 & 0 \\ 0 & 0 & 0 & 0 & c_p & -s_p \\ 0 & 0 & 0 & 0 & s_p & c_p \end{bmatrix} \tag{A.6}$$

$$[\mathbb{D}_j^q] = \begin{bmatrix} c_q^2 & 0 & s_q^2 & 0 & c_q s_q & 0 \\ 0 & 1 & 0 & 0 & 0 & 0 \\ s_q^2 & 0 & c_q^2 & 0 & -c_q s_q & 0 \\ 0 & 0 & 0 & c_q & 0 & -s_q \\ -2c_q s_q & 0 & 2c_q s_q & 0 & c_q^2 - s_q^2 & 0 \\ 0 & 0 & 0 & s_q & 0 & c_q \end{bmatrix} \tag{A.7}$$

$$[\mathbb{D}_j^r] = \begin{bmatrix} c_r^2 & s_r^2 & 0 & 0 & 0 & c_r s_r \\ s_r^2 & c_r^2 & 0 & 0 & 0 & -c_r s_r \\ 0 & 0 & 1 & 0 & 0 & 0 \\ 0 & 0 & 0 & c_r & -s_r & 0 \\ 0 & 0 & 0 & s_r & c_r & 0 \\ -2c_r s_r & 2c_r s_r & 0 & 0 & 0 & c_r^2 - s_r^2 \end{bmatrix} \tag{A.8}$$

References

References

[1] S. C. Cowin, et al., Bone mechanics handbook, CRC press, 2001.

[2] E. Hamed, I. Jasiuk, Multiscale damage and strength of lamellar bone modeled by cohesive finite elements, Journal of the Mechanical Behavior of Biomedical Materials 28 (2013) 94–110.

[3] F. Barthelat, R. Rabiei, Toughness amplification in natural composites, Journal of the Mechanics and Physics of Solids 59 (4) (2011) 829–840.

[4] J.-Y. Rho, L. Kuhn-Spearing, P. Zioupos, Mechanical properties and the hierarchical structure of bone, Medical Engineering & Physics 20 (2) (1998) 92–102.

[5] N. Reznikov, R. Shahar, S. Weiner, Bone hierarchical structure in three dimensions, Acta Biomaterialia 10 (9) (2014) 3815–3826.

[6] S. Weiner, W. Traub, Bone structure: from ångstroms to microns, The FASEB Journal 6 (3) (1992) 879–885.

[7] A. Ural, D. Vashishth, Hierarchical perspective of bone toughness–from molecules to fracture, International Materials Reviews 59 (5) (2014) 245–263.

[8] S. Weiner, W. Traub, H. D. Wagner, Lamellar bone: structure–function relations, Journal of Structural Biology 126 (3) (1999) 241–255.

[9] M.-M. Giraud-Guille, Twisted plywood architecture of collagen fibrils in human compact bone osteons, Calcified Tissue International 42 (3) (1988) 167–180.

[10] W. Landis, M. Song, A. Leith, L. McEwen, B. McEwen, Mineral and organic matrix interaction in normally calcifying tendon visualized in three dimensions by high-voltage electron microscopic tomography and graphic image reconstruction, Journal of Structural Biology 110 (1) (1993) 39–54.

[11] M. J. Olszta, X. Cheng, S. S. Jee, R. Kumar, Y.-Y. Kim, M. J. Kaufman, E. P. Douglas, L. B. Gower, Bone structure and formation: A new perspective, Materials Science and Engineering: R: Reports 58 (3-5) (2007) 77–116.

[12] P. Zioupos, J. Currey, Changes in the stiffness, strength, and toughness of human cortical bone with age, Bone 22 (1) (1998) 57–66.

[13] G. P. Parsamian, T. L. Norman, Diffuse damage accumulation in the fracture process zone of human cortical bone specimens and its influence on fracture toughness, Journal of Materials Science: Materials in Medicine 12 (9) (2001) 779–783.

[14] D. Vashishth, Hierarchy of bone microdamage at multiple length scales, International Journal of Fatigue 29 (6) (2007) 1024–1033.

[15] F. A. Sabet, A. Raeisi Najafi, E. Hamed, I. Jasiuk, Modelling of bone fracture and strength at different length scales: a review, Interface Focus 6 (1) (2016) 20150055.

[16] F. Maceri, M. Marino, G. Vairo, A unified multiscale mechanical model for soft collagenous tissues with regular fiber arrangement, Journal of Biomechanics 43 (2) (2010) 355–363.

[17] M. Marino, G. Vairo, Stress and strain localization in stretched collagenous tissues via a multiscale modelling approach, Computer Methods in Biomechanics and Biomedical Engineering 17 (1) (2014) 11–30.

[18] M. Marino, G. Vairo, Influence of inter-molecular interactions on the elasto-damage mechanics of collagen fibrils: a bottom-up approach towards macroscopic tissue modeling, Journal of the Mechanics and Physics of Solids 73 (2014) 38–54.

[19] D. Bianchi, E. Monaldo, A. Gizzi, M. Marino, S. Filippi, G. Vairo, A fsi computational framework for vascular physiopathology: a novel flow-tissue multiscale strategy, Medical Engineering & Physics 47 (2017) 25–37.

[20] A. Pandolfi, A. Gizzi, M. Vasta, A microstructural model of cross-link interaction between collagen fibrils in the human cornea, Philosophical Transactions of the Royal Society A 377 (2144) (2019) 20180079.

[21] F. Concha, D. E. Hurtado, Upscaling the poroelastic behavior of the lung parenchyma: A finite-deformation micromechanical model, Journal of the Mechanics and Physics of Solids 145 (2020) 104147.

[22] C. Morin, C. Hellmich, Z. Nejim, S. Avril, Fiber rearrangement and matrix compression in soft tissues: Multiscale hypoelasticity and application to tendon, Frontiers in Bioengineering and Biotechnology (2021) 855.

[23] Y. Kwon, B. Clumpner, Multiscale modeling of human bone, Multiscale and Multidisciplinary Modeling, Experiments and Design 1 (2) (2018) 133–143.

[24] F. Maceri, M. Marino, G. Vairo, Age-dependent arterial mechanics via a multiscale elastic approach, International Journal for Computational Methods in Engineering Science and Mechanics 14 (2) (2013) 141–151.

[25] M. Marino, G. Pontrelli, G. Vairo, P. Wriggers, A chemo-mechano-biological formulation for the effects of biochemical alterations on arterial mechanics: the role of molecular transport and multiscale tissue remodelling, Journal of The Royal Society Interface 14 (136) (2017) 20170615.

[26] M. Gierig, P. Wriggers, M. Marino, Computational model of damage-induced growth in soft biological tissues considering the mechanobiology of healing, Biomechanics and Modeling in Mechanobiology 20 (4) (2021) 1297–1315.

[27] D. Bianchi, M. Marino, G. Vairo, An integrated computational approach for aortic mechanics including geometric, histological and chemico-physical data, Journal of Biomechanics 49 (12) (2016) 2331–2340.

[28] A. Gizzi, M. L. De Bellis, M. Vasta, A. Pandolfi, Diffusion-based degeneration of the collagen reinforcement in the pathologic human cornea, Journal of Engineering Mathematics 127 (1) (2021) 1–10.

[29] C. Falcinelli, A. Di Martino, A. Gizzi, G. Vairo, V. Denaro, Mechanical behavior of metastatic femurs through patient-specific computational models accounting for bone-metastasis interaction, Journal of the Mechanical Behavior of Biomedical Materials 93 (2019) 9–22.

[30] A. Pisano, P. Fuschi, Limit analysis of human proximal femur, Journal of the Mechanical Behavior of Biomedical Materials 124 (2021) 104844.

[31] P. Gaziano, C. Falcinelli, G. Vairo, A computational insight on damage-based constitutive modelling in femur mechanics, European Journal of Mechanics – A/Solids (2022) 104538.

[32] H. A. Hogan, Micromechanics modeling of Haversian cortical bone properties, Journal of Biomechanics 25 (5) (1992) 549–556.

[33] J. Crolet, B. Aoubiza, A. Meunier, Compact bone: numerical simulation of mechanical characteristics, Journal of Biomechanics 26 (6) (1993) 677–687.

[34] P. J. Prendergast, R. Huiskes, Microdamage and osteocyte-lacuna strain in bone: a microstructural finite element analysis, Journal of Biomechanical Engineering 118 (2) (1996) 240–246.

[35] E. Giner, C. Arango, A. Vercher, F. J. Fuenmayor, Numerical modelling of the mechanical behaviour of an osteon with microcracks, Journal of the Mchanical Behavior of Biomedical Materials 37 (2014) 109–124.

[36] X. Guo, L. Liang, S. Goldstein, Micromechanics of osteonal cortical bone fracture.

[37] A. R. Najafi, A. R. Arshi, M. Eslami, S. Fariborz, M. H. Moeinzadeh, Micromechanics fracture in osteonal cortical bone: A study of the interactions between microcrack propagation, microstructure and the material properties, Journal of Biomechanics 40 (12) (2007) 2788–2795.

[38] A. Ascenzi, E. Bonucci, A. Simkin, An approach to the mechanical properties of single osteonic lamellae, Journal of Biomechanics 6 (3) (1973) 227–235.

[39] A. Ascenzi, P. Baschieri, A. Benvenuti, The bending properties of single osteons, Journal of Biomechanics 23 (8) (1990) 763–771.

[40] A. Ascenzi, E. Bonucci, The tensile properties of single osteons, The Anatomical Record 158 (4) (1967) 375–386.

[41] A. Ascenzi, P. Baschieri, A. Benvenuti, The torsional properties of single selected osteons, Journal of Biomechanics 27 (7) (1994) 875–884.

[42] G. Marotti, V. Cane, S. Palazzini, C. Palumbo, Structure-function relationships in the osteocyte.

[43] J. A. Petruska, A. J. Hodge, A subunit model for the tropocollagen macromolecule, Proceedings of the National Academy of Sciences of the United States of America 51 (5) (1964) 871.

[44] W. Landis, The strength of a calcified tissue depends in part on the molecular structure and organization of its constituent mineral crystals in their organic matrix, Bone 16 (5) (1995) 533–544.

[45] I. Jäger, P. Fratzl, Mineralized collagen fibrils: a mechanical model with a staggered arrangement of mineral particles, Biophysical Journal 79 (4) (2000) 1737–1746.

[46] R. A. Robinson, An electron-microscopic study of the crystalline inorganic component of bone and its relationship to the organic matrix, The Journal of Bone & Joint Surgery 34 (2) (1952) 389–476.

[47] A. Vercher, E. Giner, C. Arango, J. E. Tarancón, F. J. Fuenmayor, Homogenized stiffness matrices for mineralized collagen fibrils and lamellar bone using unit cell finite element models, Biomechanics and Modeling in Mechanobiology 13 (2) (2014) 437–449.

[48] S. Nikolov, D. Raabe, Hierarchical modeling of the elastic properties of bone at submicron scales: the role of extrafibrillar mineralization, Biophysical Journal 94 (11) (2008) 4220–4232.

[49] S. Torquato, Effective stiffness tensor of composite media: II. applications to isotropic dispersions, Journal of the Mechanics and Physics of Solids 46 (8) (1998) 1411–1440.

[50] R. Hill, Theory of mechanical properties of fibre-strengthened materials: I. elastic behaviour, Journal of the Mechanics and Physics of Solids 12 (4) (1964) 199–212.

[51] L. P. Kollar, G. S. Springer, Mechanics of composite structures, Cambridge university press, 2003.

[52] R. C. McPhedran, G. W. Milton, Bounds and exact theories for the transport properties of inhomogeneous media, Applied Physics A 26 (4) (1981) 207–220.

[53] J. Eischen, S. Torquato, Determining elastic behavior of composites by the boundary element method, Journal of Applied Physics 74 (1) (1993) 159–170.

[54] T. Hassenkam, G. E. Fantner, J. A. Cutroni, J. C. Weaver, D. E. Morse, P. K. Hansma, High-resolution AFM imaging of intact and fractured trabecular bone, Bone 35 (1) (2004) 4–10.

[55] E. Hamed, Y. Lee, I. Jasiuk, Multiscale modeling of elastic properties of cortical bone, Acta Mechanica 213 (1) (2010) 131–154.

[56] H. A. Lowenstam, S. Weiner, et al., On biomineralization, Oxford University Press on Demand, 1989.

[57] S. Cusack, A. Miller, Determination of the elastic constants of collagen by brillouin light scattering, Journal of Molecular Biology 135 (1) (1979) 39–51.

[58] M. J. Buehler, Nanomechanics of collagen fibrils under varying cross-link densities: atomistic and continuum studies, Journal of the Mechanical Behavior of Biomedical Materials 1 (1) (2008) 59–67.

[59] H. S. Gupta, J. Seto, W. Wagermaier, P. Zaslansky, P. Boesecke, P. Fratzl, Cooperative deformation of mineral and collagen in bone at the nanoscale, Proceedings of the National Academy of Sciences 103 (47) (2006) 17741–17746.

[60] J. L. Katz, Hard tissue as a composite material—I. Bounds on the elastic behavior, Journal of Biomechanics 4 (5) (1971) 455–473.

[61] H. Yao, L. Ouyang, W.-Y. Ching, Ab initio calculation of elastic constants of ceramic crystals, Journal of the American Ceramic Society 90 (10) (2007) 3194–3204.

[62] R. Pidaparti, A. Chandran, Y. Takano, C. Turner, Bone mineral lies mainly outside collagen fibrils: predictions of a composite model for osternal bone, Journal of Biomechanics 29 (7) (1996) 909–916.

[63] M. A. Rubin, I. Jasiuk, J. Taylor, J. Rubin, T. Ganey, R. P. Apkarian, TEM analysis of the nanostructure of normal and osteoporotic human trabecular bone, Bone 33 (3) (2003) 270–282.

[64] P. Suquet, Homogenization techniques for composite media, Springer, 1987.

[65] M. Hori, S. Nemat-Nasser, On two micromechanics theories for determining micro–macro relations in heterogeneous solids, Mechanics of Materials 31 (10) (1999) 667–682.

[66] U. Akiva, H. D. Wagner, S. Weiner, Modelling the three-dimensional elastic constants of parallel-fibred and lamellar bone, Journal of Materials Science 33 (6) (1998) 1497–1509.

[67] H. D. Wagner, S. Weiner, On the relationship between the microstructure of bone and its mechanical stiffness, Journal of Biomechanics 25 (11) (1992) 1311–1320.

[68] O. L. Katsamenis, H. M. Chong, O. G. Andriotis, P. J. Thurner, Load-bearing in cortical bone microstructure: Selective stiffening and heterogeneous strain distribution at the lamellar level, Journal of the Mechanical Behavior of Biomedical Materials 17 (2013) 152–165.

[69] F. Barthelat, Z. Yin, M. J. Buehler, Structure and mechanics of interfaces in biological materials, Nature Reviews Materials 1 (4) (2016) 1–16.

[70] P. Gaziano, C. Lorenzi, D. Bianchi, E. Monaldo, A. Dolci, G. Vairo, Mechanical performance of Anatomic-Functional-Geometry dental treatments: A computational study, Medical Engineering & Physics 86 (2020) 96–108.

[71] F. Fouchal, F. Lebon, M. L. Raffa, G. Vairo, An interface model including cracks and roughness applied to masonry, The Open Civil Engineering Journal 8 (2014) 263–271.

[72] J. C. Brewer, P. A. Lagace, Quadratic stress criterion for initiation of delamination, Journal of Composite Materials 22 (12) (1988) 1141–1155.

[73] A. Ascenzi, E. Bonucci, The compressive properties of single osteons, The Anatomical Record 161 (3) (1968) 377–391.

[74] X. N. Dong, X. Zhang, X. E. Guo, Interfacial strength of cement lines in human cortical bone, Molecular & Cellular Biomechanics 2 (2) (2005) 63.

[75] R. F. Bigley, L. V. Griffin, L. Christensen, R. Vandenbosch, Osteon interfacial strength and histomorphometry of equine cortical bone, Journal of Biomechanics 39 (9) (2006) 1629–1640.

[76] A. Ascenzi, A. Benvenuti, E. Bonucci, The tensile properties of single osteonic lamellae: technical problems and preliminary results, Journal of Biomechanics 15 (1) (1982) 29–37.

[77] M. Jirásek, Damage and smeared crack models, in: Numerical modeling of concrete cracking, Springer, 2011, pp. 1–49.

[78] W. Brekelmans, J. De Vree, Reduction of mesh sensitivity in continuum damage mechanics, Acta Mechanica 110 (1) (1995) 49–56.

[79] P. Ausiello, A. Apicella, C. L. Davidson, Effect of adhesive layer properties on stress distribution in composite restorations—a 3D finite element analysis, Dental Materials 18 (4) (2002) 295–303.

[80] W. Bonfield, C. Li, Anisotropy of nonelastic flow in bone, Journal of Applied Physics 38 (6) (1967) 2450–2455.

[81] E. A. Zimmermann, E. Schaible, H. Bale, H. D. Barth, S. Y. Tang, P. Reichert, B. Busse, T. Alliston, J. W. Ager, R. O. Ritchie, Age-related changes in the plasticity and toughness of human cortical bone at multiple length scales, Proceedings of the National Academy of Sciences 108 (35) (2011) 14416–14421.

[82] J. D. Currey, K. Brear, P. Zioupos, The effects of ageing and changes in mineral content in degrading the toughness of human femora, Journal of Biomechanics 29 (2) (1996) 257–260.

[83] M. Marino, M. von Hoegen, J. Schröder, P. Wriggers, Direct and inverse identification of constitutive parameters from the structure of soft tissues. Part 1: micro-and nanostructure of collagen fibers, Biomechanics and Modeling in Mechanobiology 17 (4) (2018) 1011–1036.

[84] M. von Hoegen, M. Marino, J. Schröder, P. Wriggers, Direct and inverse identification of constitutive parameters from the structure of soft tissues. Part 2: dispersed arrangement of collagen fibers, Biomechanics and Modeling in Mechanobiology 18 (4) (2019) 897–920.

[85] S. Farzaneh, O. Trabelsi, S. Avril, Inverse identification of local stiffness across ascending thoracic aortic aneurysms, Biomechanics and Modeling in Mechanobiology 18 (1) (2019) 137–153.

[86] F. A. Khatib, A. Gouissem, A. Eilaghi, M. Adouni, The effect of enzymatic crosslink degradation on the mechanics of the anterior cruciate ligament: A hybrid multi-domain model, Applied Sciences 11 (18) (2021) 8580.

[87] H. Gao, Application of fracture mechanics concepts to hierarchical biomechanics of bone and bone-like materials, International Journal of Fracture 138 (1) (2006) 101–137.

[88] D. Sen, M. J. Buehler, Structural hierarchies define toughness and defect-tolerance despite simple and mechanically inferior brittle building blocks, Scientific reports 1 (1) (2011) 1–9.

[89] M. Paggi, P. Wriggers, Stiffness and strength of hierarchical polycrystalline materials with imperfect interfaces, Journal of the Mechanics and Physics of Solids 60 (4) (2012) 557–572.